Applied Thermal Engineering 256 (2024) 124083

Contents lists available at ScienceDirect

Applied Thermal Engineering

journal homepage: www.elsevier.com/locate/ate

Research Paper

A comprehensive numerical study on heat transfer and friction characteristics of offset-strip fins

Mattia Grespan [a,*], Luigi Calò [a,b], Lorenzo Carlesso [a], Adriano Leonforte [a], Diego Angeli [c]

[a] DISMI - Dipartimento di Scienze e Metodi dell'Ingegneria, Università di Modena e Reggio Emilia, Via Amendola 2, Pad. Buccola, 42122, Reggio Emilia, Italy
[b] VEMA Industries S.p.A., Via Guido Rossa 8, 43058, Sorbolo, Italy
[c] Centro Interdipartimentale EN&TECH, Piazzale Europa 1, 42124, Reggio Emilia, Italy

ARTICLE INFO

Keywords:
Offset-strip fins
Staggered fins
Head losses
Heat transfer
DOE
Response surfaces
Correlations
CFD

ABSTRACT

Offset-strip fins are among the most used geometries in compact heat exchangers. The geometric and flow parameters of the fins affect their heat transfer effectiveness and head losses. Hence, accurate predictive models are needed to guide the design process. However, most of the correlations available in the literature are valid only for a limited set of geometric configurations and flow regimes. This work discusses the derivation of multivariate response surfaces for the equivalent Darcy and Colburn factors in offset-strip fins. These surfaces feature clear applicability ranges and extend over wide Reynolds and Prandtl number ranges ($50 \leq Re \leq 12000$, $0.71 \leq Pr \leq 190$). In addition, a novel empirical model for the Prandtl number scaling exponent is proposed. The analysis is carried out through a Design of Experiment approach, performed with computational techniques. Each numerical experiment is carried out by CFD analysis of a periodic fin geometry. The obtained response surfaces approximate CFD results with a mean deviation of ±8.4%. Moreover, application of the correlations to the analysis of complete heat exchangers issued mean and maximum deviations of ±7.8% and ±20%, respectively, thus highlighting the usefulness of the proposed models for the accurate modelling of offset-strip fins in heat transfer applications.

1. Introduction

1.1. Engineering and technical background

In today's industrial landscape, improving the efficiency of thermal processes and cycles is of paramount importance, due to rising energy costs and environmental concerns. Heat exchangers play a critical role in most industrial thermal processes and improving their performance through advanced design techniques is of increasing technical interest [1]. In compact heat exchangers used for the thermal management of specific systems, such as components of electric power trains in automotive applications and power generation units, Offset-Strip Fins, commonly referred to by the acronym OSF, are among the most used extended surfaces. OSFs, compared to conventional straight channels, feature augmented heat transfer effectiveness, which is mainly achieved by the periodic disruption and regrowth of boundary layers along the fin walls. Secondary contributions to the heat transfer enhancement are given by a slightly increased surface area, and by the periodic vortex shedding at the trailing edges of the fins, which favours fluid mixing. Of course, the improved heat transfer performance is accompanied by an increase in the head losses, which can be significant in certain configurations. Therefore, it is essential to select the most appropriate geometric parameters in order to obtain acceptable compromises between heat transfer effectiveness and pressure losses [2]. This is an intricate task, as the geometry of offset-strip fins is defined by a wide number of parameters including, but not limited to, the fin pitch x, the fin height y, the offset length l, and the wall thickness t. Further complications arise from the large variety of fluids that can be used with these fins. These include air and other gases which are typical of the aerospace and power generation industries, as well as water mixtures and hydraulic or lubricating oils, which are more common in heavy-duty vehicle applications, such as agricultural and earth-moving equipment.

Although over the years many studies have been carried out on staggered fin arrays, the resulting predictive models can be considered valid and reliable only within narrow ranges of dimensional and flow parameters. For this reason, the present analysis is aimed at the integration of the results obtained thus far through a Design Of Experiment (DOE) procedure, carried out by means of computational techniques. The main goal of this work consists in obtaining a set of continuous response surfaces for the equivalent Darcy friction

* Corresponding author.
E-mail address: mattia.grespan@unimore.it (M. Grespan).

https://doi.org/10.1016/j.applthermaleng.2024.124083
Received 29 February 2024; Received in revised form 12 July 2024; Accepted 31 July 2024
Available online 5 August 2024

Nomenclature

Latin letters

A	Area [m^2]
b_m	Coefficients in Eqs. (9) and (10)
c	Vertical crush [m]
c_p	Specific heat [J kg^{-1} K^{-1}]
C	Heat capacity rate [W K^{-1}]
d_m	Coefficients in Eqs. (32) and (33)
D_h	Hydraulic diameter [m]
f	Equivalent Darcy friction factor [–]
H	Heat exchanger height [m]
j	Colburn factor [–]
k_n	Coefficients in Eqs. (11), (34), and (35)
l	Offset length [m]
L	Heat exchanger core length [m]
n	Prandtl number scaling exponent [–]
N_{ch}	Number of internal channels [–]
Nu	Nusselt number [–]
NTU	Number of transfer units [–]
p	Fluid pressure [Pa]
P	Wetted perimeter [m]
Pr	Prandtl number [–]
q	Heat flux [W m^{-2}]
$\dot{Q}$	Heat [W]
r	External corner radius [m]
Re	Reynolds number uy/ν [–]
s	Smoothing function
S	Heat exchanger thickness [m]
St	Stanton number [–]
t	Fin thickness [m]
T	Temperature [K]
$\vec{u}$	Fluid velocity [m s^{-1}]
U	Overall heat transfer coefficient [W m^{-2} K^{-1}]
W	Manifold width [m]
x	Fin pitch [m]
y	Fin height [m]

Greek letters

β	Concentrated loss coefficient [–]
β_r	Blockage ratio [–]
ε	Effectiveness [–]
λ	Thermal conductivity [W m^{-1} K^{-1}]
ν	Kinematic viscosity [m^2 s^{-1}]
ρ	Density [kg m^{-3}]
ϑ	Dimensionless temperature difference [–]
σ	Smooth step sharpness
χ	Generic independent variable

Subscripts

b	Bulk
ch	Channel
ext	External
f	Fluid
F	Fanning
he	Heat exchanger
i	Inlet
int	Internal
l	Laminar
o	Outlet
ov	Overlap
rs	Response surface
s	Solid
t	Turbulent
w	Wall

Superscripts

*	Dimensionless

factor f and the Colburn factor j, with suitable accuracy levels over a comprehensive part of the geometric and flow parameter space. These response surfaces, in the form of multivariate correlations, could also be employed for the geometric optimisation of heat exchangers for a wide range of industrial applications. Furthermore, this work provides for the first time a derivation of a Prandtl number scaling exponent, which is specific to offset-strip fins, and computed as a function of the geometrical parameters.

1.2. Literature survey

One of the most relevant texts regarding the design of heat exchangers is the one by Kays and London [3], in which the authors provided a large experimental data set for large variety of fin geometries, including offset-strip fins. Analogous experimental data about actual fin cores can be found in [4]. The first predictive models for the thermohydraulic performance of OSFs were introduced by Manson [5]. Other very well-established correlations are those proposed by Wieting [6], which consist of piecewise defined power laws obtained from experimental tests on 22 fin cores carried out in laminar and turbulent regimes. Wieting suggested extrapolating the laminar and turbulent curves to determine the values of f and j in the transition region. Joshi and Webb [7] developed an analytical model for the determination of heat transfer and friction performance of offset-strip fins in laminar flow, and a semi-empirical model for turbulent flow. Both models accounted for the thickness of fin walls, and for microscopic geometric features such as surface roughness and imperfections that arise from the manufacturing process. These models featured remarkable accuracy levels (±20%), however they also featured a complex formulation, so the authors introduced more convenient power laws, analogous to the ones proposed by Wieting [6], but with improved accuracy thanks to a larger database, and an empirical relation for the transition Reynolds number as a function of the geometrical parameters. Joshi and Webb conducted their experiments with an aqueous ethylene glycol solution as the working fluid, and considered additional data about air flows available in the literature, thus the derived correlations can be considered reasonably valid over the range $0.71 \leq \mathrm{Pr} \leq 7$. Mochizuki et al. [8] tested several offset-strip and slotted fin cores, considering air as the working fluid, and developed correlations in the form proposed by Wieting [6]. A similar work is the one by Dubrovsky and Vasiliev [9]. Manglik and Bergles [10] presented a revision of the data available in the literature by attempting to unify the definitions of hydraulic diameter and heat transfer area, as these are not given in some of the works or their formulation appears unclear. The authors focused on the transition region and concluded that, for their configurations, the equivalent friction factor and the Colburn factor vary continuously with Re and that there is no noticeable discontinuity in the transition region. Finally, the authors mentioned the problem of a high-frequency sound that can be emitted by some fin cores at certain flow regimes, but did not elaborate further. Similar high-intensity tonal noise emissions were observed by Roesler et al. [11]. Dong et al. [12] obtained accurate correlations (±10% deviations) by introducing an additional parameter to account for entrance effects in the fin cores. Kim et al. [13] investigated offset-strip fin performance by means of computational methods. The authors tested several turbulence models based on the eddy viscosity approach, including the standard $k-\varepsilon$, realisable $k-\varepsilon$, and the $k-\omega$ SST. The latter was found to be the most accurate with respect to the experimental results presented by Manglik and Bergles [10]. In addition, the $k-\omega$ SST turbulence model

showed promising accuracy levels when used to model oscillatory flows with steady state simulations [14]. Kim et al. [13] also introduced an additional geometric parameter called blockage ratio which indicates the portion of the fin frontal area occupied by the fin walls. The authors also investigated the effects of the Prandtl number on heat transfer performance, conducting CFD analyses with Pr-values ranging from 0.72 to 50. Significant variations of the Colburn factor were found, suggesting that using the traditional Pr exponent (1/3) for the computation of the Colburn factor is not an adequate approximation. Yang and Li [15] studied entire offset-strip channels by means of steady-state CFD analyses to account for entrance effects. The authors used the blockage ratio like Kim et al. [13], but with a slightly different definition. On the basis of these correlations, Yang et al. [16] proposed an original approach based on relative entropy generation to determine optimal OSF geometric and flow parameters. In an effort to obtain improved estimates of OSF performance, Yang et al. [17] introduced the actual fin efficiency parameter to overcome the major limitations and simplifying assumptions introduced by the classical fin efficiency definition [18]. Peng et al. [19] proposed an innovative offset-strip fin architecture obtained by slightly bending an array of plain rectangular channels. Michna et al. [20] investigated the thermo-hydraulic performance of OSFs at very high Reynolds number values $10000 \leq \mathrm{Re}_{D_h} \leq 120000$, associated with automotive and aerospace applications where maximum compactness is sought at the expense of increased fan pumping power. Significant deviations were observed when these results were compared with those obtained by extrapolating the correlations of Manglik and Bergles [10] and Muzychka and Yovanovich [21].

Several authors investigated the effect of the Prandtl number of the working fluid on the heat transfer performance of offset-strip fins. Tinaut et al. [22] carried out experiments with lubricating oil, concluding that for such fluids the Prandtl number scaling exponent is closer to 0.4, as supposed to the traditionally used value of 1/3. Hu and Herold [23,24] tested several working fluids with Prandtl number values ranging from 3 to 150, and showed that the use of correlations developed on the basis of gas flows can lead to significant overestimations of the Colburn factor, possibly causing significant design errors. Guo et al. [25] developed correlations for heat transfer and pressure losses for carbon steel OSFs operating with lubricating oil, concluding that the thermohydraulic performance is mainly influenced by the aspect ratio and offset length [26]. In a following contribution [27] the authors investigated the effects on heat transfer performance given by the flow angle, which provided maximum improvement at 45°. Xiang, Du, and Zhao [28] developed empirical correlations from numerical analyses performed with Pr-values ranging from 2 to 13, considering the effects of fin offset, unlike most authors. Du et al. [29] employed a Genetic Algorithm to optimise the performance of an oil-to-air heat exchanger equipped with trapezoidal OSFs. Furthermore, the authors compared the j and f values of the optimised solution with those from the models by Wieting [6] and Manglik and Bergles [10], noting significant deviations attributed to the adoption of a trapezoidal cross section and the high Pr-value of the considered working fluid. Recently, Kedam et al. [30] proposed an empirical predictive model based on an Artificial Neural Network (ANN), that was trained on a set of heat transfer and pressure loss data in air flows. This modelling approach allowed for the prediction of j and f values with deviations of 1%–2% with respect to the data points. Similarly, Chandan et al. [31] employed a stacking ensemble modelling approach and machine learning algorithms to derive a predictive model for the friction factor of OSF-equipped micro channels, with a mean absolute error of 0.403%.

Offset-strip fins are also widely used in multi-phase flows, such as refrigerant cycles in electric vehicles heat pumps [32], as they offer significant improvements in terms of heat transfer effectiveness compared to plain channels [33]. Several authors investigated evaporation and condensation phenomena in OSFs considering different refrigerants such as R133 [34], HFE-7100 [35], R134a [36], and others [37–40].

The careful analysis of the literature shows that in almost every work, different definitions are adopted for the hydraulic diameter, the heat transfer area and the other geometric parameters, and it is easy to fall into errors because the same symbols are used to describe different quantities. This makes the comparison between results difficult and sometimes impossible, as some authors do not specify how they computed the reference velocity, the hydraulic diameter and the heat transfer area. Therefore, it is necessary to be cautious and pay attention to what each research group identifies as reference quantities. Furthermore, it is clear that heat transfer performance is strongly influenced by the working fluid, i.e. by its Prandtl number [41], but up to now a single and robust approach to address this problem has not been proposed yet. Finally, it is interesting to note how the proposed correlations become increasingly more complex as new parameters are added through the years, suggesting that no definitive conclusions have yet been drawn on the heat transfer and friction properties of offset-strip fins, and that there is still ample room for new contributions to the subject.

1.3. Modelling approach

The present research deals with the analysis of the single-phase thermohydraulic performance of offset-strip fins with straight vertical walls, centred or symmetric offset, and filleted corners. The basic geometric parameters such as fin pitch, fin height, and wall thickness are defined as in the work by Yang and Li [15], but in this case different symbols are used to avoid any ambiguity. In addition, analytical expressions for hydraulic diameter and heat transfer area are provided to allow for their exact computation.

A Design of Experiment analysis of heat transfer performance and pressure losses is carried out by means of computational techniques. The values of geometric and flow parameters are selected considering the most recurrent configurations in real industrial applications. A full factorial DOE is performed with respect to the dimensionless fin pitch, the offset length, and the flow regime, which is defined by pairs of Reynolds and Prandtl numbers. The resulting configurations are studied by means of CFD analyses of basic fin modules obtained by exploiting the periodicity of the geometry and of the flow along the streamwise and spanwise directions. The solution to the incompressible and periodic flow is attained by means of a validated conjugate heat transfer solver, based on a Finite Volume discretisation of the governing equations. Integral results on pressure losses and heat transfer effectiveness are presented by an equivalent Darcy friction factor and average Nusselt number, which are based on the fin height. These values are used to derive separate response surfaces for laminar and turbulent flow, which are then combined by means of a smoothing hyperbolic tangent function. The effect of the Prandtl number on heat transfer performance is manged by introducing the Colburn factor, and by computing the Pr scaling exponent as a function of the geometric parameters of the fins by performing dedicated CFD analyses. The numerical results and response surfaces are compared with some of the most relevant correlations available in the literature for a selected group of geometric configurations.

Finally, the response surfaces obtained in this work are validated by computing the internal head losses and overall heat transfer rates of three oil coolers, which feature offset-strip fins within the internal channels. These results are compared with the available experimental data and numerical results obtained in a previous work, by performing dedicated CFD analyses for the examined fin geometry.

2. Problem statement

This work is focused on offset-strip fins with straight vertical walls and symmetric or centred offset. The front and top views of the examined offset-strip fin geometry are depicted in the drawings of Fig. 1, along with the key dimensional parameters. The fin pitch,

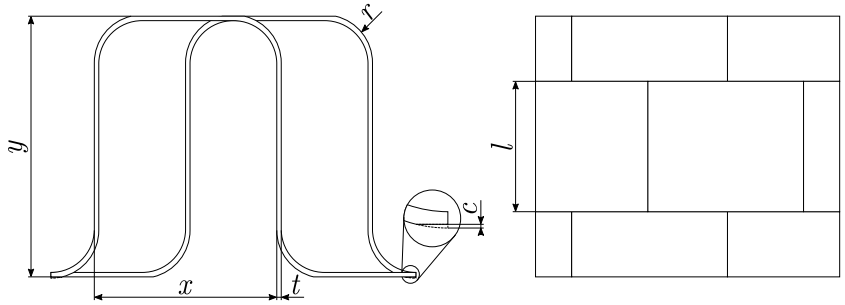

Fig. 1. Front and top views of the examined offset-strip fin geometry, along with the most significant dimensions.

denoted by x, is the distance between two consecutive vertical walls, including the thickness of one of the two walls t. The external corner radius between vertical and horizontal fin walls is denoted by r, while the fin height is identified by y. During the production process of compact heat exchangers the fins undergo mechanical deformations as a result of the stacking of finned plates and brazing sheets. The most marked effect consists of a vertical crushing, which is reproduced by cutting the outer fillet radii by an amount c, so that they are no longer tangent to the horizontal walls. c is set to 0.5% of the fin height to introduce a small deformation, that is not too excessive for the configurations with small pitch values. The centred offset constraint determines a relationship between fin pitch, the maximum value of the external fillet radius, and wall thickness:

$$x = 4\,r_{\max} - 2\,t. \tag{1}$$

The reference flow cross-sectional area and heat trasnfer surface are depicted in the drawings of Fig. 2, while their analytical definitions are reported in Appendix A.

3. Numerical methods

3.1. Governing equations

Offset-strip fins are modelled by means of basic unit geometries, which are obtained by exploiting the periodicity of the geometry and flow along the streamwise and spanwise directions. The flow is assumed incompressible, and periodic between the inlet and outlet sections of the examined periodic modules. The fluid velocity, pressure, and temperature fields are obtained from the numerical solution of the steady-state momentum, continuity, and energy equations, which in dimensionless form read:

$$\begin{cases} \dfrac{\partial u_i^* u_j^*}{\partial x_j^*} = -\dfrac{\partial p^*}{\partial x_i^*} + \dfrac{\partial}{\partial x_j^*}\left[\left(\dfrac{1}{\mathrm{Re}} + \nu_t^*\right)\dfrac{\partial u_i^*}{\partial x_j^*}\right] \\ \dfrac{\partial u_i^*}{\partial x_i^*} = 0 \\ \dfrac{\partial T^* u_j^*}{\partial x_i^*} = \dfrac{\partial}{\partial x_j^*}\left[\left(\dfrac{1}{\mathrm{Re\,Pr}} + \dfrac{\nu_t^*}{\mathrm{Pr}_t}\right)\dfrac{\partial T^*}{\partial x_j^*}\right] \end{cases} \tag{2}$$

The temperature field within the fin walls is derived from the numerical solution of the steady state heat equation.

$$\frac{\partial}{\partial x_j^*}\left(\lambda_s^* \frac{\partial T^*}{\partial x_j^*}\right) = 0 \tag{3}$$

The fin height y is assumed as the reference length of the problem, while the velocity scale, defined as the integral mean velocity over the inlet surface, is taken as unitary. The Reynolds number is defined as follows:

$$\mathrm{Re} = \frac{\bar{u}_i\, y}{\nu}. \tag{4}$$

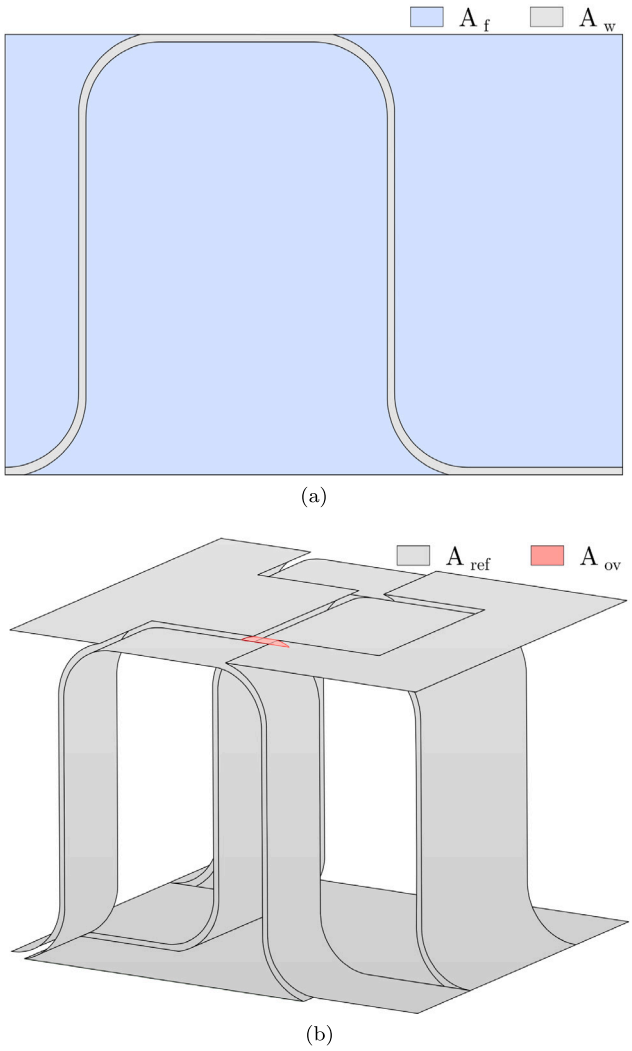

Fig. 2. Flow cross-sectional area (a) and heat transfer area (b) of the examined offset-strip fins.

The dimensionless thermal conductivity of the fin walls is derived by scaling the thermal conductivity of aluminium by the one of the neighbouring fluid:

$$\lambda_s^* = \frac{\lambda_{\mathrm{Al}}}{\lambda_f}, \tag{5}$$

the values of λ of aluminium and all the considered fluids are reported in Table 1. At $\mathrm{Re} \geq 1000$, the k-ω SST turbulence model [42], coupled with a low-Reynolds wall modelling approach, is employed to compute eddy viscosity ν_t^* in Eqs. (2), as it is the turbulence model that gives the

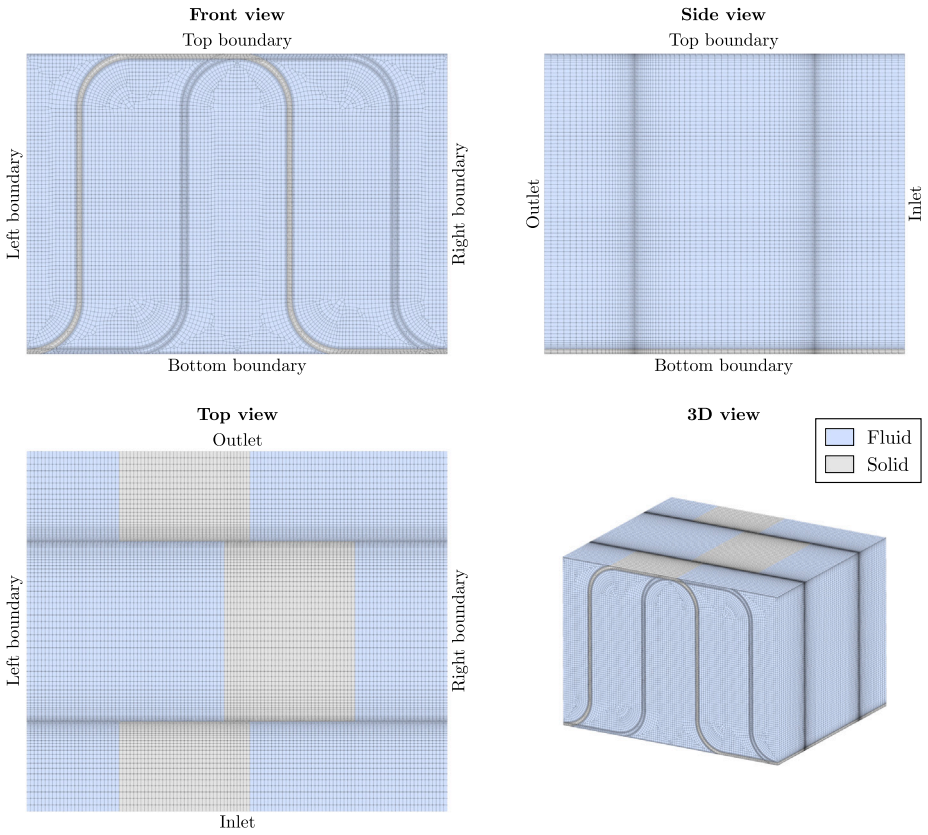

Fig. 3. Selected views of one of the generated computational grids, related to the geometrical configuration defined by $x^* = 0.7$ and $l^* = 0.6$.

Table 1
Reference values of thermal conductivity of aluminium and oil, water, and air flows.

	Aluminium	Oil	Water	Air
λ [W m^{-1} K^{-1}]	237.0	0.129	0.609	0.024

best agreement between numerical and experimental results according to Kim et al. [13]. On the other hand, for all flows at Re $\leq$ 200 laminar analyses are carried out, therefore, in this case eddy viscosity is set to zero. At Re = 500 laminar simulations are performed as long as a satisfactory degree of numerical convergence is achieved, i.e. when all residuals are of the order of 10^{-6}. Otherwise, the turbulence model is employed. In the turbulent analyses, a unitary value for the turbulent Prandtl number $\mathrm{Pr_t}$ is considered, on the basis of the Reynolds analogy.

3.2. Boundary conditions

Fully developed flow conditions are attained by enforcing suitable field mapping boundary conditions for the velocity and temperature fields, between the inlet and outlet sections. At each iteration of the solution algorithm, the values of dimensionless velocity and temperature at each cell centre on the outlet patch are applied to the respective cell centre on the inlet patch, after being scaled to maintain the desired integral mean values at the inlet: $\bar{u}_{\mathrm{i}}^* = 1$ and $\overline{T}_{\mathrm{i}}^* = 0$. At the outlet, the surface mean pressure is set to a zero reference value $\bar{p}_{\mathrm{o}}^* = 0$, while at the inlet a zero gradient condition is applied to pressure. Periodic conditions are enforced along the spanwise direction. At the top and bottom boundaries a uniform entering heat flux is imposed: $q''^* = 1$. At the walls, no-slip conditions are applied to the velocity field and a zero pressure gradient is imposed. Finally, continuity of temperature and heat flux is enforced at all fluid-solid interfaces. Table 2 summarises the boundary conditions described herein.

3.3. Spatial discretisation

A Finite Volume conjugate heat transfer solver, previously validated in [43], and implemented in the open source software OpenFOAM 7 [44], is employed for the numerical analyses. The previously discussed dimensionless framework is implemented by setting up the thermophysicalProperties file as shown in Appendix B. Spatial discretisation of convective terms is addressed with second-order upwind schemes, while diffusive terms are handled with central differencing schemes with explicit non-orthogonality correction. The momentum and continuity equations are decoupled by means of the SIMPLE method [45]. The computational domains are generated using an automated mesh generation script implemented in Glyph, the Tcl-based scripting language for the commercial meshing tool Pointwise. Meshing strategies and parameters are chosen with aim of obtaining grids with satisfactory quality indicators, while maintaining a relatively simple implementation of the automated scripts and limiting the number of cells of each computational mesh. On average, the resulting computational grids feature mean values of equiangle skewness of 0.045, mean mesh non-orthogonality of 5.75 degrees, and a number of cells of roughly 2 millions. Fig. 3 shows one of the generated computational grids, where the fluid and solid regions are clearly highlighted.

3.4. Mesh sensitivity analysis

The dependence of numerical results on the computational grid is assessed by comparing local velocity and temperature results, and integral results on head losses and heat transfer, which are represented by an equivalent Darcy friction factor and Nusselt number (for their definitions refer to Section 5), obtained from three different grids featuring the same topology. The analysis is conducted considering an oil flow at Re = 50 and an air flow at Re = 12000, the latter representing the worst case scenario in terms of the computation of

Table 2
Boundary conditions applied to the inlet, outlet, left and right boundaries, and top and bottom surfaces in fluid and solid regions.

Boundaries		Inlet	Outlet	Left/right	Top/bottom	Fluid-solid interface
Fluid	$\vec{u}^*$	Mapped	Zero-gradient	Periodic	No-slip	No-slip
	p^*	Zero-gradient	Fixed mean	Periodic	Zero-gradient	Zero-gradient
	T^*	Mapped	Zero-gradient	Periodic	Fixed gradient	Heat flux continuity
Solid	T^*	Zero-gradient	Zero-gradient	Periodic	Fixed gradient	Heat flux continuity

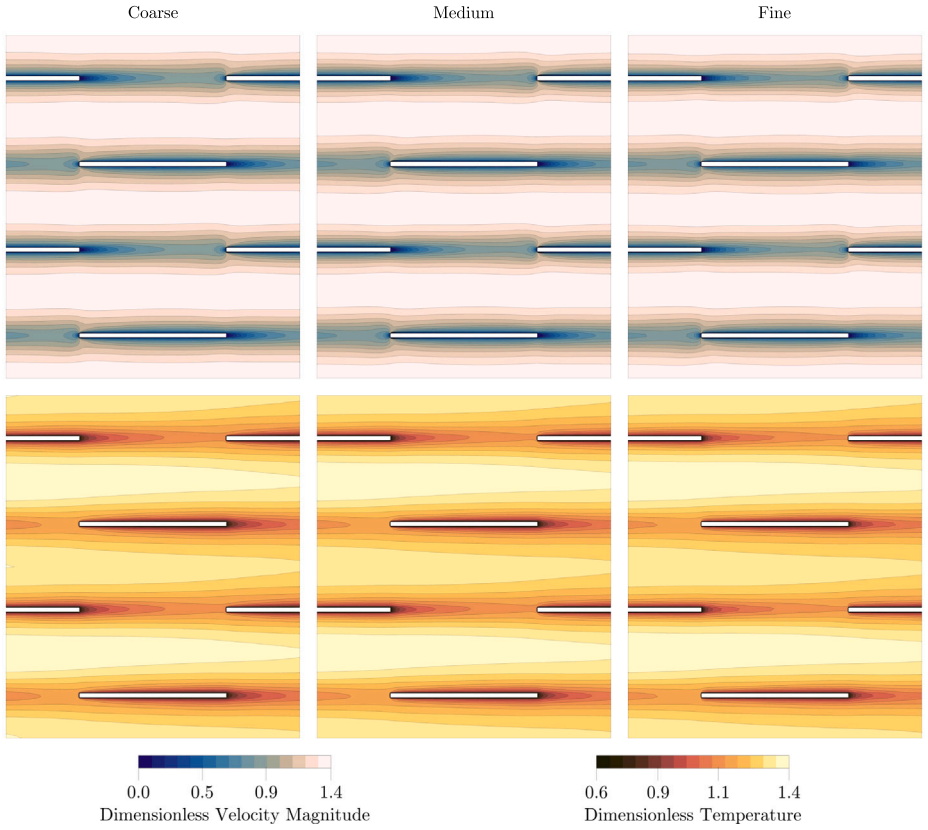

Fig. 4. Contours of dimensionless velocity magnitude and temperature difference obtained from the coarse, medium, and fine meshes at Re = 12000 and Pr = 0.71.
Source: Colour schemes from [46].

wall normal gradients. Table 3 shows f and Nu values, along with the mean dimensionless wall distance, that are obtained from three computational meshes of an offset-strip fin with $x^* = 0.7$ and $l^* = 0.6$. The deviations in friction factor and Nusselt number related to each grid are computed by taking the value from the previous mesh as a reference. In laminar flow, at Re = 50, the three meshes produce very close results, showing deviations well below 0.2% when comparing integral results between the medium and fine grids. At Re = 12000 these deviations increase up to 7.2% for f and 3.3% for Nu. Fig. 4 compares local results on dimensionless velocity magnitude and temperature difference (see Section 5) obtained from the three grids at Re = 12000, by means of contour plots on cross sections positioned at half of the fin height. The three velocity contours feature similar distributions, with the most noticeable differences found in the wakes between two successive fin walls, thus affecting the prediction of pressure losses as seen in Table 3. On the other hand, in the temperature contours the most noticeable differences are spotted in the sub-channels generated by the staggered fin profiles.

Although the deviations observed between results from the medium and fine grids are not insignificant, the meshing parameters associated with the medium grid are selected for the development of all computational grids for the following CFD analyses. This choice is aimed at achieving an acceptable tradeoff between accuracy and the required computational effort, which is particularly relevant in this case since the total number of CFD analyses amounts to 704 (see Section 4). On average, the medium sized grid requires roughly 27 core-hours for the solution of a single flow rate, while the fine grid requires a much higher 865 core-hours, representing an increase in computational time which is arguably not justified by the accuracy improvements shown in Table 3. Furthermore, it should be stressed that the deviations observed at Re = 12000 really represent the most penalising scenario, while at lower Reynolds values much lower differences between integral results are expected, as confirmed by the numerical analyses carried out at Re = 50.

Table 3
Friction factor, Nusselt number, and mean dimensionless wall distance values obtained from the coarse, medium, and fine computational meshes of a fin with $x^* = 0.7$ and $l^* = 0.6$.

Re	Grid	Δ^*	$\bar{y}^+$	f	Nu	Δf	ΔNu
50	Coarse	0.014	–	3.43	14.9	–	–
	Base	0.007	–	3.44	15.0	0.4%	0.24%
	Fine	0.0035	–	3.44	15.0	−0.02%	0.16%
12 000	Coarse	0.014	1.44	0.16	71.1	–	–
	Base	0.007	0.64	0.14	67.1	−9.2%	−5.6%
	Fine	0.0035	0.06	0.13	64.8	−7.2%	−3.3%

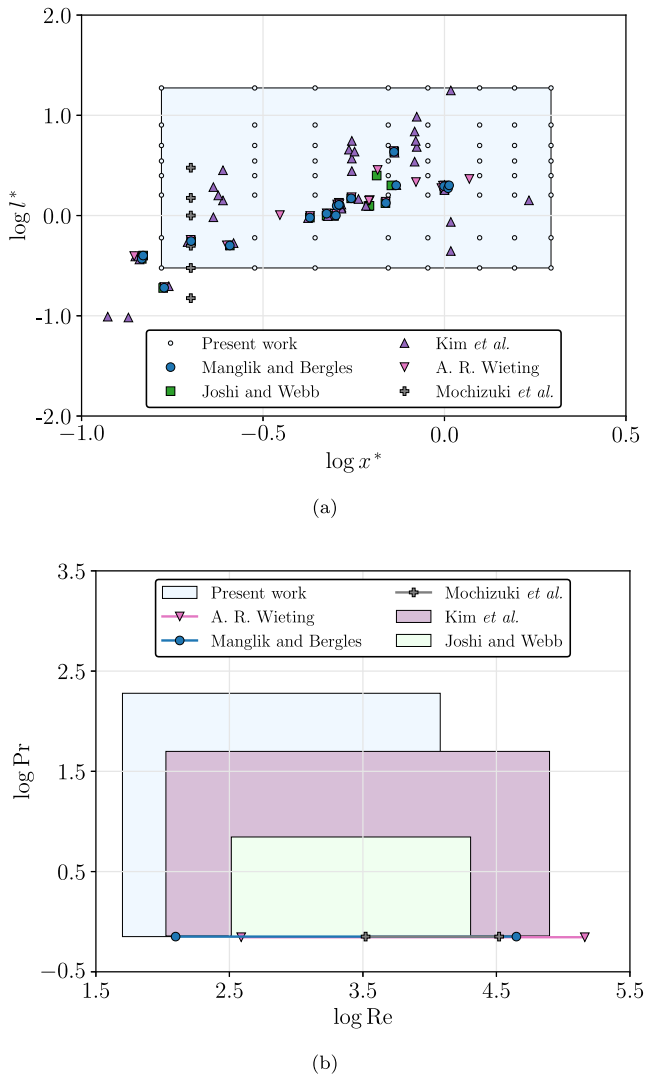

Fig. 5. Comparison between the dimensional (a) and flow (b) parameters considered in this work with those analysed in previous works in the literature.

4. Design of experiment

The dependence of the thermohydraulic performance of OSFs on geometric and flow parameters is evaluated by means of a Design of Experiment procedure. The dimensionless fin pitch and offset length are assumed as the most influential geometric parameters [26], instead the fillet radius and wall thickness are considered of secondary importance. The levels of the dimensional parameters x^*, l^* and of the flow parameters, i.e. pairs of Re and Pr values, are chosen considering a set of configurations which are representative of real industrial applications, including coolers for hydraulic and lubricating oils, water radiators, and air to air heat exchangers [47]. Thus, eight levels are selected for x^* and l^*, and eleven different flows are taken into account. The fillet radius is varied indirectly by computing it as a function of fin pitch and wall thickness, according to Eq. (1). This strategy allows for the removal of one geometric parameter from the DOE, which vastly reduces the number of numerical analyses to perform. On the other hand, the effects of pitch and radius variations on thermohydraulic performance may be confounded, as the fillet radius is aliased by Eq. (1). In this case, this is deemed acceptable as the fillet radius is most likely to have a lower order influence on head losses and heat transfer with respect to the fin pitch [26]. The dimensionless wall thickness t^* is kept constant at a value of 0.017, again in an effort to reduce the number of simulations, and because in real applications the choice of the wall thickness values is limited, due to the commercially available aluminium sheets and the need to satisfy criteria of structural integrity and mechanical resistance of the heat exchangers.

Table 4
Selected levels for geometric and flow factors.

x^*	0.166	0.3	0.44	0.7	0.9	1.25	1.56	1.966	
l^*	0.3	0.6	1.6	2.5	3.5	5.0	8.0	18.75	
Re	50	100	200	500	1000	2000	3000	5000	12 000
Pr	190	190	190	190	7	7 - 0.71	7 - 0.71	0.71	0.71

In an effort to obtain an accurate sampling of the parameter space a full factorial DOE with respect to the factors x^* and l^* and the (Re, Pr) couples is performed. This is equivalent to performing a fractional factorial DOE with respect to x^*, l^*, r^*, Re, and Pr. Table 4 reports the levels chosen for each geometric and flow factor, while the number of numerical analyses performed amounts to 704.

The configurations studied in the present work are compared to those analysed in some of the most relevant works available in the literature in the plots of Fig. 5. The geometric configurations studied in the literature are spread very unevenly over the geometric parameter space, and some configurations are repeated among the different works. By examining the points distribution in Fig. 5(a) it is clear that the correlations proposed in the literature cannot be considered universal. Furthermore, given the irregularity of the distribution, it is also difficult to guess their actual field of applicability and to discern in which parts of the geometrical parameter space they represent an extrapolation. A clear advantage of the DOE approach presented in this work is the clear identification of the ranges of validity of the obtained response surfaces (Section 6), which are represented by the shaded areas of the plots of Fig. 5. Nevertheless, such an advantage comes at the cost of a large computational effort. Moreover, an analysis of this scope would be practically unfeasible if conducted by means of experimental techniques, which were used the most in the papers available in the literature.

The graph of Fig. 5(b) clearly shows that most of the works available in the literature deal with air flows (Pr = 0.71) only, therefore the resulting correlations are to be considered reliable only for gas flows, as usually specified by the authors. The work presented by Kim et al. [13] is one of the few that considers higher Prandtl number fluids (up to 50), in fact the associated correlations are those with the widest field of applicability.

In closing, the present analysis should be seen as integrative with respect to what has been done so far by other researchers, as the main objective is to cover the space of dimensional and flow parameters in a more uniform and systematic way, in order to obtain more general and reliable response surfaces. Nevertheless, this work is by no means definitive, given the large number and variability of the dimensional and flow parameters associated with the application of offset-strip fins in compact heat exchangers.

5. Numerical results

Numerical flow field results are hereby presented by means of dimensionless velocity and temperature contour plots, associated with cross sections positioned at the fins half height. The dimensionless temperature difference is computed according to its classic definition [18]:

$$\vartheta = \frac{\overline{T}_w - T}{\overline{T}_w - \overline{T}_b}, \tag{6}$$

where $\overline{T}_w$ is the integral mean temperature over the heat transfer area A_{ref}, while $\overline{T}_b$ is computed as the mean of the mass flow weighted averages of temperature on the inlet and outlet surfaces. Figs. 6 and 7 depict an example of the aforementioned contour plots related to

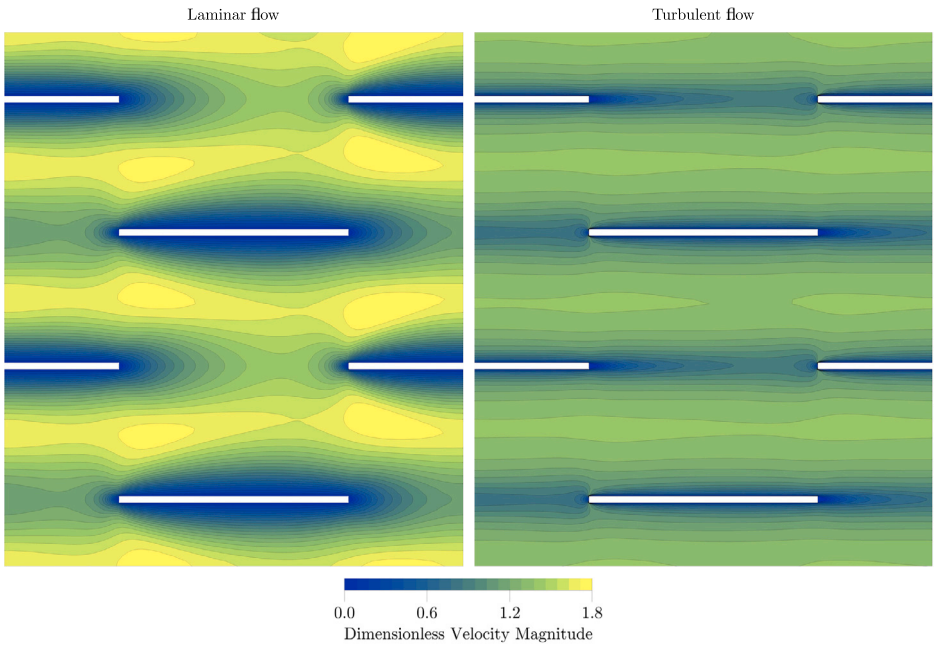

Fig. 6. Contour plots of dimensionless velocity magnitude on height centred cross sections, related to a laminar (left) and turbulent flow (right). *Source:* Colour scheme from [46].

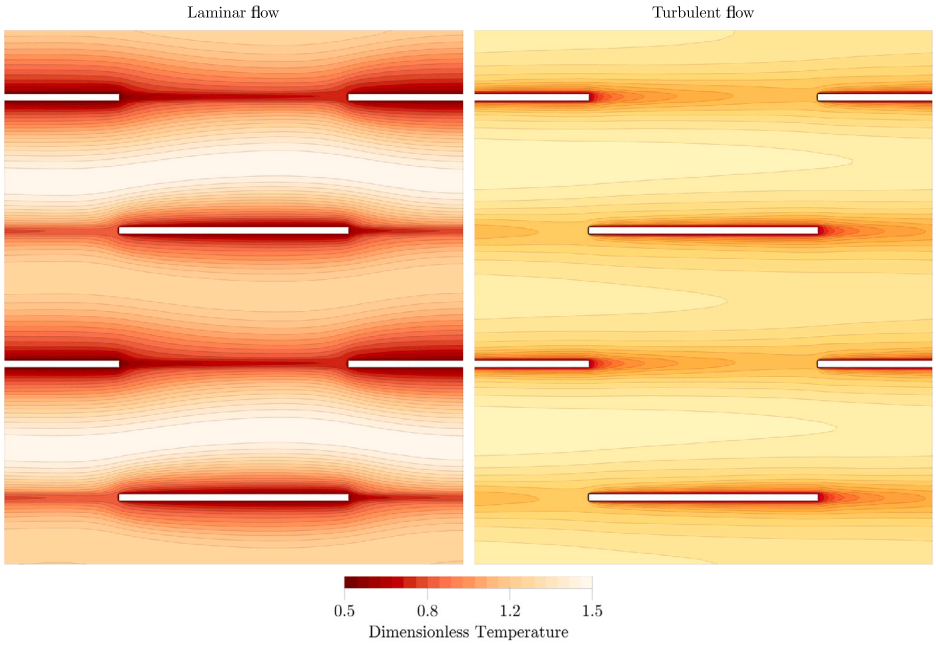

Fig. 7. Contour plots of dimensionless temperature difference on height centred cross sections, related to a laminar (left) and turbulent flow (right).

an offset-strip fin with $x^* = 0.7$ and $l^* = 0.6$. Furthermore, two reference flows are considered: a laminar oil flow (Re = 50, Pr = 190) and a turbulent air flow (Re = 12000, Pr = 0.71). As expected, in laminar regime the development of boundary layers along the fin walls is much more evident with respect to the case of turbulent flow, and coherently, greater velocity values are noted near the leading edge of the fins. The presence of the fillet radii determines an asymmetry between the two flow passages formed at each interruption of the profiles, resulting in slight asymmetries in the velocity and temperature fields. It is interesting to note that even though in laminar regime the velocity distribution features very mild asymmetries, the temperature field presents a really marked asymmetric distribution, suggesting that this behaviour is emphasised by large values of Prandtl number. In the turbulent regime, the wakes formed past each fin wall are much smaller along the spanwise direction, than those generated in laminar flow. However, these wakes are never completely dissipated due to the short offset length. In this case, the flow asymmetries are more evident in the velocity field than in the temperature one.

Fig. 8 shows contour plots of Turbulent Kinetic Energy (TKE) on a longitudinal cross section and in the fluid volume near the fin walls, along with the distributions of local Nusselt number and friction coefficient. The 3D iso-surfaces of TKE in Fig. 8 are referred to TKE-values of 0.033, 0.035, and 0.046. The maximum values of TKE are noticed near the leading edge of the walls and in the wakes. Furthermore, it can be observed that regions exhibiting high TKE values, indicative of high turbulent dissipation, correspond to areas where higher values of the

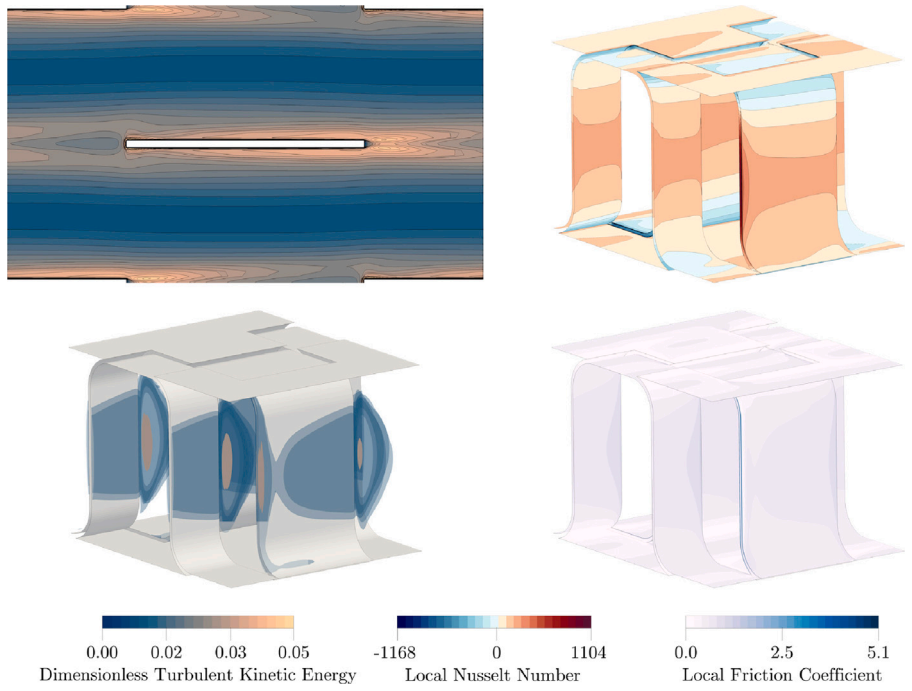

Fig. 8. Distributions of turbulent kinetic energy, local Nusselt number, and local friction coefficient, obtained at Re = 12000 and Pr = 0.71.

local friction coefficient can be observed on the fin walls. As expected, the largest values of local Nusselt number are observed near the leading edge of the walls, while far lower values are noted on the side walls. The regions of high local Nu are broadly consistent with zones of large turbulent kinetic energy.

Integral head losses and heat transfer rates are evaluated by means of an equivalent Darcy friction factor and mean Nusselt number. The equivalent friction factor f is derived from the Darcy-Weisbach formula, where the reference length is the fin height y:

$$f = \frac{y(\bar{p}_\mathrm{i} - \bar{p}_\mathrm{o})}{l\,\rho\,\bar{u}_\mathrm{i}^2}\,, \tag{7}$$

overbars denote integral mean values over inlet (i) and outlet (o) sections. The mean Nusselt number over the heat transfer area is:

$$\mathrm{Nu} = \frac{\dot{Q}\,y}{\lambda\,A_\mathrm{ref}\,(\overline{T}_\mathrm{w} - \overline{T}_\mathrm{b})}\,, \tag{8}$$

where $\dot{Q}$ stands for the heat entering the system through the top and bottom surfaces. Fig. 9 shows contour plots depicting the distributions of f and Nu over the examined configuration space, related to a laminar flow at Re = 50. As expected, the equivalent friction factor decreases with increasing fin pitch and offset length. Moreover, at small pitch values and for large l^*-values the contour lines become almost vertical, underlining the reduced dependence of f on the offset length in this region of the parameter space. Conversely, this effect is not as pronounced for large pitch values, since the friction factor maintains a more marked sensitivity with respect to the offset length. In laminar regime, the mean Nusselt number shows comparable trends to those of the friction factor, but in this case a much more pronounced dependence on the offset length is noted, especially towards the lower end of the considered fin pitch range. Fig. 10 shows analogous contour plots, related to turbulent a flow at Re = 12000. The friction factor distribution closely resembles its laminar flow counterpart, while the mean Nusselt number features a local minimum for the values $x^* = 0.166$ and $l^* = 1.6$. This behaviour is investigated further by comparing the local Nusselt number distributions of three fins with a value of pitch of 0.166 and l^*-values of 0.6, 1.6, and 2.5. The black rectangles in Fig. 11 highlight the subtle differences between the obtained Nu distributions in the central region of the upper surface of the fin profiles. The configuration with $l^* = 1.6$ exhibits a notable absence of the high Nu strip that is clearly spotted in the other two configurations. Moreover, as emphasised by the magenta rectangles, the fins with l^*-values of 1.6 and 2.5 feature regions of low Nusselt number in proximity to the fillet radius on the lower portion of the side walls. The fin with $l^* = 0.6$ features the largest of these regions and also lacks the region where large values of Nusselt number are spotted in the configuration with $l^* = 2.5$. The observed differences between the three Nu distributions are consistent with the Nusselt number minimum present in Fig. 10(b). Moreover, the latter appears to be related to the presence of the fillet radius between the vertical and horizontal walls of the fins, since most of the deviations between the distributions in Fig. 11 are observed in correspondence of the radiused corners.

6. Derivation of response surfaces

The derivation of the response surfaces presents several challenges: first and foremost, the number of data points is quite large, and accurately representing them without the use of overly complex models is a challenging task. Furthermore, the selected levels for the geometric and flow factors are unevenly distributed, and they cover extremely wide ranges spanning several orders of magnitude, especially in the case of the Reynolds and Prandtl numbers.

An additional challenge arises from the laminar-turbulent transition, that occurs at different Reynolds numbers depending on the geometric parameters: in fins with the minimum pitch value ($x^* = 0.166$) the transition Reynolds number is between 500 to 1000, while for all the other configurations it is located roughly between 250 to 500. The offset length has a comparatively minor influence on the transition point with respect to the pitch, as it affects the transition of only a few fin configurations that feature a pitch of $x^* = 0.44$. In the frame of the derivation of response surfaces and correlations, the laminar-turbulent transition is usually addressed by deriving response surfaces for each flow regime and prescribing the appropriate ranges of validity. Although this is a very straightforward and robust approach, it leads to piecewise-defined response surfaces, which may not be suitable for optimisation procedures as they are not continuous functions.

The response surfaces presented in the following are obtained by defining objective functions and fitting them to data points by means

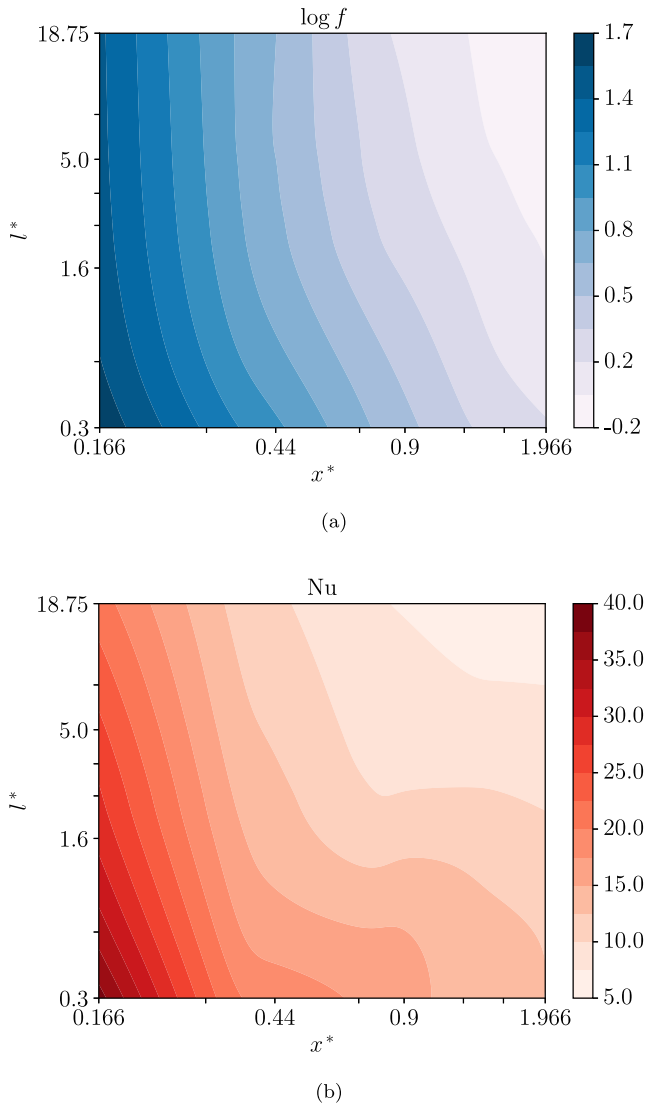

Fig. 9. Contour plots of equivalent Darcy friction factor (a), and mean Nusselt number (b), obtained from the CFD analyses performed at Re = 50 and Pr = 190. In these plots the x^* and l^* axes are in logarithmic scale. However, the labels are in linear scale for better readability.

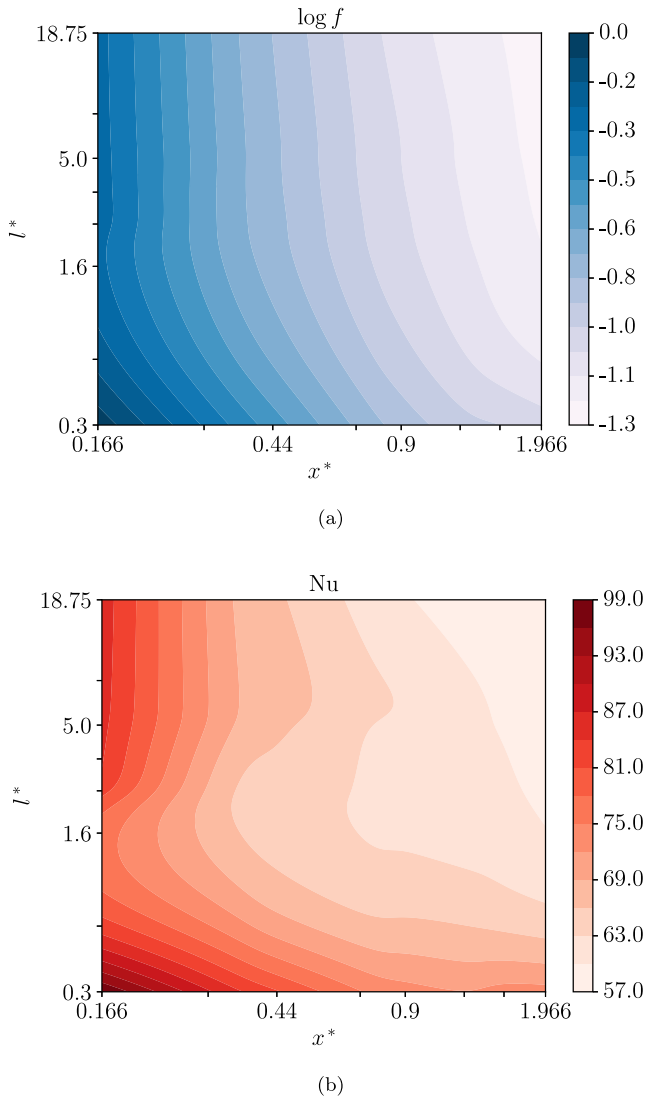

Fig. 10. Contour plots of equivalent Darcy friction factor (a), and mean Nusselt number (b), obtained from the CFD analyses performed at Re = 12000 and Pr = 0.71. In these plots the x^* and l^* axes are in logarithmic scale. However, the labels are in linear scale for better readability.

of a variant of the Levenberg–Marquardt algorithm [48], that is implemented in the SciPy library [49]. Although response surfaces obtainded by least-squares regression may not be as accurate in approximating the base data as those obtained by ANN-based approaches, they are used in this analysis because of their advantages in terms of ease of implementation and application. All data points in the range $50 \leq \mathrm{Re} \leq 200$ are employed for the fit of the laminar functions while the ones in the range $1000 \leq \mathrm{Re} \leq 12000$ are used for the turbulent fit. The data points obtained at $\mathrm{Re} = 500$ are used to fit the laminar or turbulent response surfaces depending on the specific geometric configuration. The transition is managed by combining the response surfaces obtained for laminar and turbulent regimes by means of a smoothing function, based on the hyperbolic tangent, that is used to connect the two surfaces around the suited transition point.

6.1. Equivalent darcy friction factor

The dependence of the equivalent Darcy friction factor on the Reynolds number is modelled by polynomial functions in log–log scale:

$$\log f_l = b_1 \log \mathrm{Re} + b_2 \,, \tag{9}$$

$$\log f_t = b_3 \log^{-0.48} \mathrm{Re} + b_4. \tag{10}$$

These formulations are used to correlate results on both pressure losses and heat transfer (see Section 6.2) as they provide very good accuracy levels when used for extended surfaces [47]. The values of the b_m coefficients found in Eqs. (9) and (10) are obtained from the following relation, as a function of the geometrical parameters:

$$b_m = k_1 (x^*)^{k_2} + k_3 x^* + k_4 \log l^* + k_5 l^* + k_6. \tag{11}$$

Eq. (11) is formulated by progressively adding polynomial and logarithmic based terms as long as these provide significant improvements to the accuracy of the response surface. The values of the k_n coefficients are determined through the aforementioned least-squares-based curve fitting procedure, and their values are listed in Table 5. In order to suitably combine Eqs. (9) and (10) a smoothing function based on the hyperbolic tangent is formulated:

$$s = \frac{1}{2}\left[1 + \tanh\left(\frac{\chi - \chi_0}{\sigma}\right)\right] . \tag{12}$$

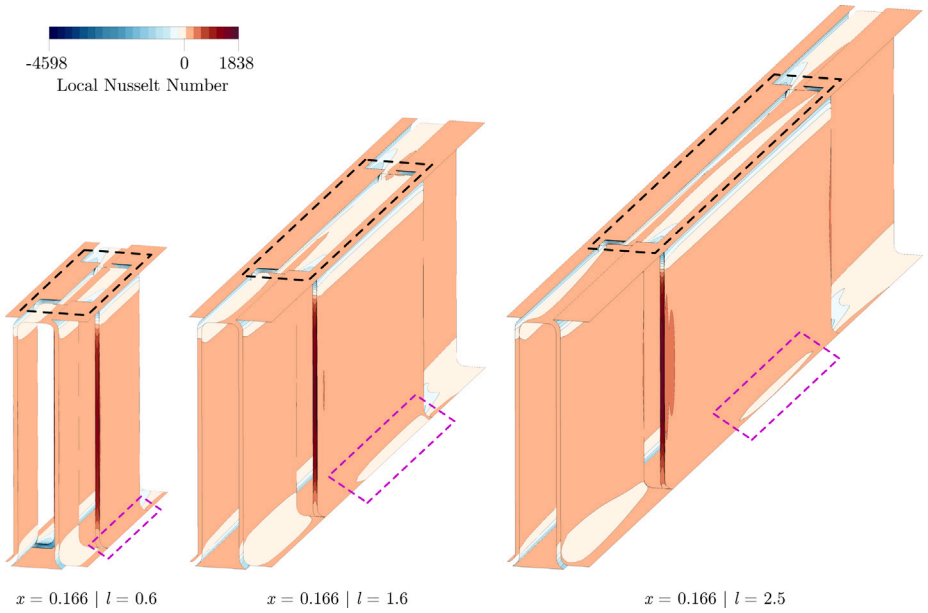

Fig. 11. Distributions of local Nusselt number related to offset-strip fins with pitch $x^* = 0.166$ and values of offset length of 0.6 (left), 1.6 (middle), and 2.5 (right), obtained at Re = 12000 and Pr = 0.71.

In Eq. (12) χ stands for the generic independent variable, χ_0 locates the smooth step on the independent variable axis, while σ determines the sharpness of the transition. The laminar and turbulent response surfaces (Eqs. (9) and (10)) are combined into a single equation by employing a variant of Eq. (12) centred at the transition Reynolds number $\mathrm{Re}_{\mathrm{trans}}$:

$$\log f = s_{\mathrm{Re}} \log f_{\mathrm{t}} + (1 - s_{\mathrm{Re}}) \log f_{\mathrm{l}} , \tag{13}$$

$$s_{\mathrm{Re}} = \frac{1}{2}\left[1 + \tanh\left(\frac{\log \mathrm{Re} - \log \mathrm{Re}_{\mathrm{trans}}}{0.08}\right)\right] . \tag{14}$$

The transition Reynolds number is in turn determined by applying the previously defined smoothing function (Eq. (12)) between the Re-values of 750 and 350 which have been designated as transition values, on the basis of the fin dimensionless pitch alone.

$$\mathrm{Re}_{\mathrm{trans}} = s_{x^*}\, 350 + (1 - s_{x^*})\, 750 , \tag{15}$$

$$s_{x^*} = \frac{1}{2}\left[1 + \tanh\left(\frac{x^* - 0.166}{1.1}\right)\right] . \tag{16}$$

The values of transition Reynolds number in Eq. (15), along with the values of σ in Eqs. (14) and (16) were selected with the aim of maximising the accuracy of the overall response surface with respect to the data points. The plots of Fig. 12 display CFD results for the equivalent Darcy friction factor, the obtained response surface (Eq. (13)), and a comparison with some of the most relevant correlations available in the literature. The displayed configurations cover the limits of the geometric parameter ranges and their median values. First of all, near the transition, a notable discontinuity between the laminar and the turbulent friction factor distributions is noted, as suggested by many authors [6–8], but in contrast with the results proposed by Manglik and Bergles [10], who argue that a smooth transition from laminar to turbulent of the friction factor should be observed. This is what prompted the use of the previously discussed smoothing technique, that appears adequate to correctly represent the transition for the examined configurations, as the mean deviation between the response surface and the data points is of 8.45%, as seen in Fig. 15(a).

The numerical results and response surface obtained in this work are compared with some of the most relevant correlations available in the literature including the ones from:

Table 5
Values of k_n coefficients in Eq. (11).

	k_1	k_2	k_3	k_4	k_5	k_6
b_1	−345.50	1.00033743	345.5969	0.0651851	−0.00681313	−0.9987
b_2	4421.93	1.00032627	−4423.93	−0.367102	0.020911319	3.76899
b_3	−4091.5	0.00026439	0.820411	−0.282540	0.017530123	4095.36
b_4	1356.77	1.00001750	−1356.95	−0.049099	−0.00012869	−3.1953

- Joshi and Webb [7]
  laminar flow: $\mathrm{Re}_{D_\mathrm{h}} \le \mathrm{Re}^*_{D_\mathrm{h}}$

$$f_{\mathrm{F}} = 8.12\, \mathrm{Re}_{D_\mathrm{h}}^{-0.74} \left(\frac{l}{D_\mathrm{h}}\right)^{-0.41} \alpha^{-0.02} \tag{17}$$

  turbulent flow: $\mathrm{Re}_{D_\mathrm{h}} \ge \mathrm{Re}^*_{D_\mathrm{h}} + 1000$

$$f_{\mathrm{F}} = 1.12\, \mathrm{Re}_{D_\mathrm{h}}^{-0.36} \left(\frac{l}{D_\mathrm{h}}\right)^{-0.65} \left(\frac{t}{D_\mathrm{h}}\right)^{0.17} \tag{18}$$

- Manglik and Bergles [10]

$$f_{\mathrm{F}} = 9.6243\, \mathrm{Re}_{D_\mathrm{h}}^{-0.7422}\, \alpha^{-0.1856}\, \delta^{0.3053}\, \gamma^{-0.2659} \times \left[1 + 7.669 \cdot 10^{-8}\, \mathrm{Re}_{D_\mathrm{h}}^{4.429}\, \alpha^{0.920}\, \delta^{3.767}\, \gamma^{0.236}\right]^{0.1} , \tag{19}$$

- Mochizuki et al. [8]
  laminar flow: $\mathrm{Re}_{D_\mathrm{h}} < 2000$

$$f_{\mathrm{F}} = 5.55 \left(\frac{l}{D_\mathrm{h}}\right)^{-0.32} \alpha^{-0.092}\, \mathrm{Re}_{D_\mathrm{h}}^{-0.67} \tag{20}$$

  turbulent flow: $\mathrm{Re}_{D_\mathrm{h}} \ge 2000$

$$f_{\mathrm{F}} = 0.83 \left(\frac{l}{D_\mathrm{h}} + 0.33\right)^{-0.5} \left(\frac{t}{D_\mathrm{h}}\right)^{0.534} \mathrm{Re}_{D_\mathrm{h}}^{-0.20} \tag{21}$$

- Wieting [6]
  laminar flow: $\mathrm{Re}_{D_\mathrm{h}} \le 1000$

$$f_{\mathrm{F}} = 7.661 \left(\frac{l}{D_\mathrm{h}}\right)^{-0.384} \alpha^{-0.092}\, \mathrm{Re}_{D_\mathrm{h}}^{-0.712} \tag{22}$$

  turbulent flow: $\mathrm{Re}_{D_\mathrm{h}} \ge 2000$

$$f_{\mathrm{F}} = 1.136 \left(\frac{l}{D_\mathrm{h}}\right)^{-0.781} \left(\frac{t}{D_\mathrm{h}}\right)^{-0.534} \mathrm{Re}_{D_\mathrm{h}}^{-0.198} \tag{23}$$

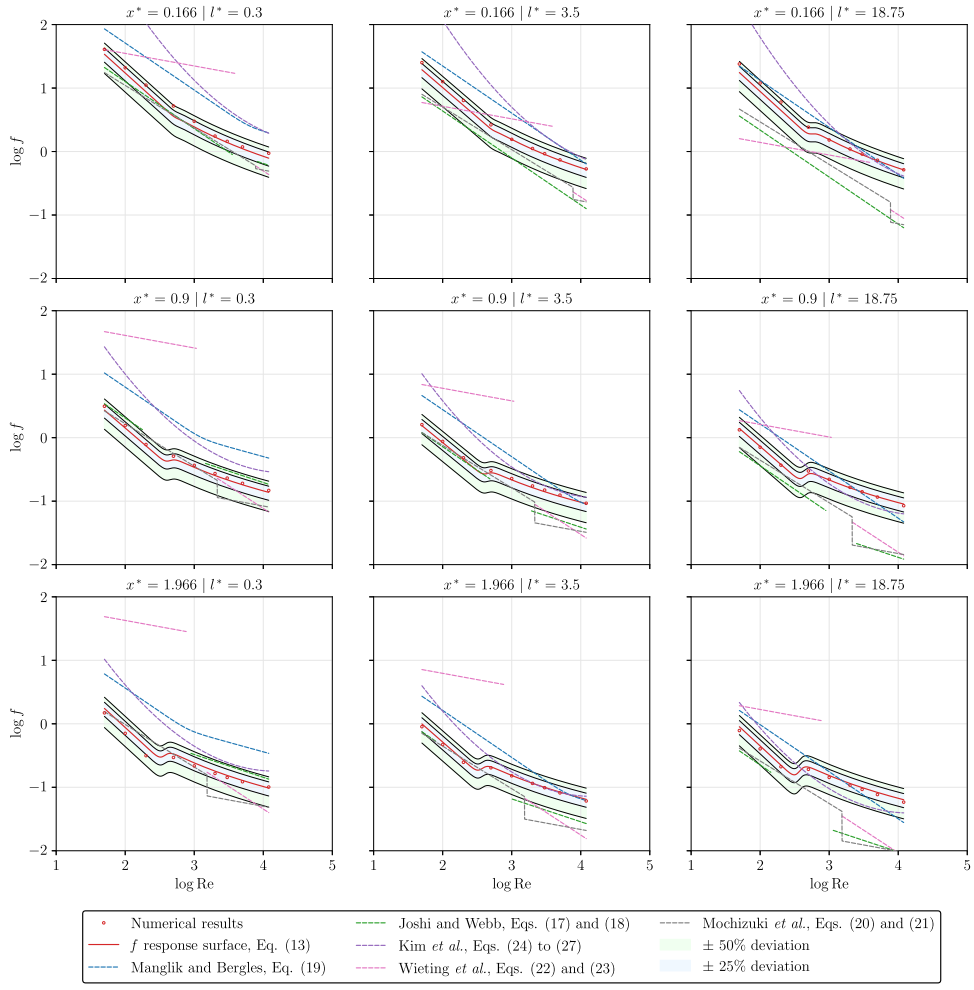

Fig. 12. Equivalent Darcy friction factor: numerical results, developed response surface, and a comparison with the most relevant correlations from the literature for nine selected geometric configurations.

- Kim et al. [13]

for $\beta_r < 20\%$

$$f_F = e^{7.91}\,\alpha^{-0.159}\,\delta^{0.358}\,\gamma^{-0.033}\,\mathrm{Re}_{D_h}^{0.126\,\ln \mathrm{Re}_{D_h} - 2.3} \tag{24}$$

for $20\% \le \beta_r < 25$

$$f_F = e^{9.36}\,\alpha^{-0.0025}\,\delta^{-0.0373}\,\gamma^{1.85}\,\mathrm{Re}_{D_h}^{0.142\,\ln \mathrm{Re}_{D_h} - 0.623} \tag{25}$$

for $25\% \le \beta_r < 30\%$

$$f_F = e^{5.58}\,\alpha^{-0.36}\,\delta^{0.552}\,\gamma^{-0.521}\,\mathrm{Re}_{D_h}^{0.111\,\ln \mathrm{Re}_{D_h} - 1.87} \tag{26}$$

for $30\% \le \beta_r \le 35\%$

$$f_F = e^{4.84}\,\alpha^{-0.48}\,\delta^{0.347}\,\gamma^{0.511}\,\mathrm{Re}_{D_h}^{0.0891\,\ln \mathrm{Re}_{D_h} - 1.49} \tag{27}$$

Eqs. from (17) to (27) are defined in terms of the dimensionless parameters α, β_r, δ, and γ which are:

$$\begin{aligned} \alpha &= \frac{x-t}{y-t}\,, \\ \beta_r &= \left(1 - \frac{1}{1+\alpha\gamma+\gamma+\alpha\gamma^2}\right)\,, \\ \delta &= \frac{t}{l}\,, \\ \gamma &= \frac{t}{x-t}\,. \end{aligned} \tag{28}$$

The comparison with the correlations from the literature is carried out by appropriately scaling the resulting values, to represent them in the frame of reference selected in this work. In particular, the Reynolds number is multiplied by the ratio between the hydraulic diameter and fin height y, and by the ratio between the flow cross sections to correct for the reference length and velocity. The resulting f values are then scaled by the y/D_h ratio to match the reference length selected in this work. From the results, it is clear that, although various correlations have been developed over the years, none of them can be considered as universal, as the observed deviations change substantially depending on the geometric configuration. Although the correlations by Joshi and Webb [7] have a rather simple formulation, they show decent accuracy levels with respect to the numerical results, especially for small values of the fin pitch and offset length. On the other hand, other correlations featuring similar formulations such as those of Wieting [6] and Mochizuki et al. [8] show far lower accuracy levels. The relations by Manglik and Bergles [10] and Kim et al. [13] have much more complex formulations, but this does not always translate into improved accuracy levels, as these two correlations produce similar estimations that tend to be better aligned with CFD results at large x^* and l^* values. As mentioned previously in Section 4, it is difficult to understand the cases in which the correlations from the literature represent extrapolations with respect to their actual validity ranges, and this could explain the very uneven accuracy levels observed in this comparison.

6.2. Colburn factor

Compared to friction and pressure losses, heat transfer effectiveness depends on one additional flow parameter, namely the Prandtl number.

Traditionally, the dependence of the Nusselt number with respect to the Prandtl number is managed by introducing the Colburn factor:

$$j = \frac{\mathrm{Nu}}{\mathrm{Re}\,\mathrm{Pr}^{n}} = \mathrm{St}\,\mathrm{Pr}^{n+1}\,, \tag{29}$$

where n is the scaling exponent for the Prandtl number, which is usually set to 1/3 in most applications. Kays and London [3] discussed the validity of this assumption by comparing results from analytical laminar boundary layer solutions and turbulent flows in round tubes. The authors determined that the 1/3 power law is a reasonable approximation to scale heat transfer results related to gas flows with $0.5 \le \mathrm{Pr} \le 1.0$. However, they also questioned the use of this approach outside of gas flows and further suggested that the correct scaling exponent may depend on the particular geometry of the problem.

Following the suggestions from Kays and London, in this work the Prandtl scaling exponent is determined by performing four sets of CFD analyses at the Re-values of 2000 and 3000 and Pr-values of 0.71 and 7.0. The Prandtl exponent related to each geometric configuration is determined by the following equation:

$$n = \frac{\log \mathrm{Nu}\big|_{\mathrm{Pr}=7} - \log \mathrm{Nu}\big|_{\mathrm{Pr}=0.71}}{\log 7 - \log 0.71}. \tag{30}$$

the results are then averaged over the two considered Re-values to derive the final n distribution. Fig. 13(a) shows the contour plot of the Prandtl number exponent obtained from CFD results scaled by its canonical value 1/3. Most of the geometric configurations feature n-values very different from 1/3: for fins with small pitch and offset length the scaling exponent is about half of its canonical value, while it is twice that for configurations with large x^*-values. The classical value of 1/3 appears as a good approximation only for a limited number of configurations, which are identified by the white region in the plot of Fig. 13(a). Lastly, it is interesting to note that the sensitivity of the scaling exponent with respect to the offset length is pronounced only for small pitch values, while it almost disappears as x^* approaches its maximum value.

The CFD derived n-values are also employed to derive a correlation as a function of the dimensional parameters:

$$n = (0.259\,(l^*)^{-1/3} + 0.072)\,\log x^* + 0.044\,\log l^* + 0.569\,. \tag{31}$$

Eq. (31) allows to obtain the value of the Prandtl exponent with a very good approximation, as the average deviation with respect to the CFD results is less than 4% (Fig. 13(b)). Eq. (31) is a good approximation for $0.71 \le \mathrm{Pr} \le 7$ and $2000 \le \mathrm{Re} \le 3000$, while outside of these ranges this relation should be used with care if employed to scale heat transfer results unrelated to this work, as lower accuracy levels could be observed. In the present work these uncertainties are avoided by consistently using these n-values to compute the values of Colburn factor for all the considered flows, and purposely deriving correlations for the resulting j-values. This approach allows for the perfect alignment of heat transfer results in turbulent regime, i.e. for water and air flows, while noticeable discontinuities are expected between laminar (hydraulic oil) and turbulent results. Nevertheless, an accurate response surface for heat transfer performance can still be obtained by managing any jump or discontinuity by means of the smoothing function that was employed for the equivalent friction factor in Section 6.1. Of course, having an accurate description about the distribution of the Pr scaling exponent over the whole Reynolds and Prandtl numbers ranges would be ideal, but this would require a much higher computational effort.

The laminar and turbulent response surfaces for the Colburn factor are derived by means of the same procedure employed for the friction factor in Section 6.1:

$$\log j_{\mathrm{l}} = d_1\,\log^{0.2}\mathrm{Re} + d_2 \tag{32}$$

$$\log j_{\mathrm{t}} = d_3\,\log^{2}\mathrm{Re} + d_4 \tag{33}$$

Table 6
Values of k_n coefficients in Eqs. (34) and (35).

	k_1	k_2	k_3	k_4	k_5	k_6	k_7
d_1	50.1014	−46.8119	1.06548	−0.0633	0.07918	1.06718	−8.5546
d_2	18.2244	−24.6789	0.76276	0.07360	−0.3988	−0.8820	10.3469
d_3	−11.656	0.000139	−6.7022	0.01874	0.29932	18.3093	–
d_4	1.4508×10^{-18}	−21.3283	45.7714	0.03263	−3.6445	−47.141	–

The values of the d_m coefficients found in Eqs. (32) and (33) are expressed as a function of the geometric parameters by the two following relations:

$$d_1,\, d_2 = k_1\,x^* + k_2\,(x^*)^{k_3} + k_4\,l^* + k_5\log l^* + k_6\log x^*\log l^* + k_7\,, \tag{34}$$

$$d_3,\, d_4 = k_1\,(x^*)^{k_2} + k_3\,(l^*)^{k_4} + k_5\log l^* + k_6\,; \tag{35}$$

where the values of k_n coefficients are again determined via the curve fitting procedure described in the introductory part of Section 6. The resulting k_n-values are reported in Table 6.

The laminar and turbulent correlations are combined by means of the same smoothing function used for the equivalent Darcy friction factor (see Eq. (14)). The transition Reynolds number is again derived by means of Eqs. (15) and (16), and the final response surface assumes the familiar form:

$$\log j = s_{\mathrm{Re}}\,\log j_{\mathrm{t}} + (1 - s_{\mathrm{Re}})\,\log j_{\mathrm{l}}. \tag{36}$$

The charts of Fig. 14 show numerical j factor results and a comparison with some of the most relevant correlations developed through the years:

- Joshi and Webb [7]
  laminar flow: $\mathrm{Re}_{D_\mathrm{h}} \le \mathrm{Re}^*_{D_\mathrm{h}}$

$$j = 0.53\,\mathrm{Re}_{D_\mathrm{h}}^{-0.5}\left(\frac{l}{D_\mathrm{h}}\right)^{-0.15}\alpha^{-0.14}\,, \tag{37}$$

  turbulent flow: $\mathrm{Re}_{D_\mathrm{h}} \ge \mathrm{Re}^*_{D_\mathrm{h}} + 1000$

$$j = 0.21\,\mathrm{Re}_{D_\mathrm{h}}^{-0.40}\left(\frac{l}{D_\mathrm{h}}\right)^{-0.24}\left(\frac{t}{D_\mathrm{h}}\right)^{0.02} \tag{38}$$

- Manglik and Bergles [10]

$$j = 0.6522\,\mathrm{Re}_{D_\mathrm{h}}^{-0.5403}\,\alpha^{-0.1541}\,\delta^{0.1499}\,\gamma^{-0.0678} \times \left[1 + 5.269\cdot 10^{-5}\,\mathrm{Re}_{D_\mathrm{h}}^{1.340}\,\alpha^{0.504}\,\delta^{0.456}\,\gamma^{-1.055}\right]^{0.1}\,, \tag{39}$$

- Mochizuki et al. [8]
  laminar flow: $\mathrm{Re}_{D_\mathrm{h}} < 2000$

$$j = 1.37\left(\frac{l}{D_\mathrm{h}}\right)^{-0.25}\alpha^{-0.184}\,\mathrm{Re}_{D_\mathrm{h}}^{-0.67} \tag{40}$$

  turbulent flow: $\mathrm{Re}_{D_\mathrm{h}} \ge 2000$

$$j = 1.17\left(\frac{l}{D_\mathrm{h}} + 3.75\right)^{-1}\left(\frac{t}{D_\mathrm{h}}\right)^{0.089}\mathrm{Re}_{D_\mathrm{h}}^{-0.36} \tag{41}$$

- Wieting [6]
  laminar flow: $\mathrm{Re}_{D_\mathrm{h}} \le 1000$

$$j = 0.483\left(\frac{l}{D_\mathrm{h}}\right)^{-0.162}\alpha^{-0.184}\,\mathrm{Re}_{D_\mathrm{h}}^{-0.536} \tag{42}$$

  turbulent flow: $\mathrm{Re}_{D_\mathrm{h}} \ge 2000$

$$j = 0.242\left(\frac{l}{D_\mathrm{h}}\right)^{-0.322}\left(\frac{t}{D_\mathrm{h}}\right)^{0.089}\mathrm{Re}_{D_\mathrm{h}}^{-0.368} \tag{43}$$

- Kim et al. [13]

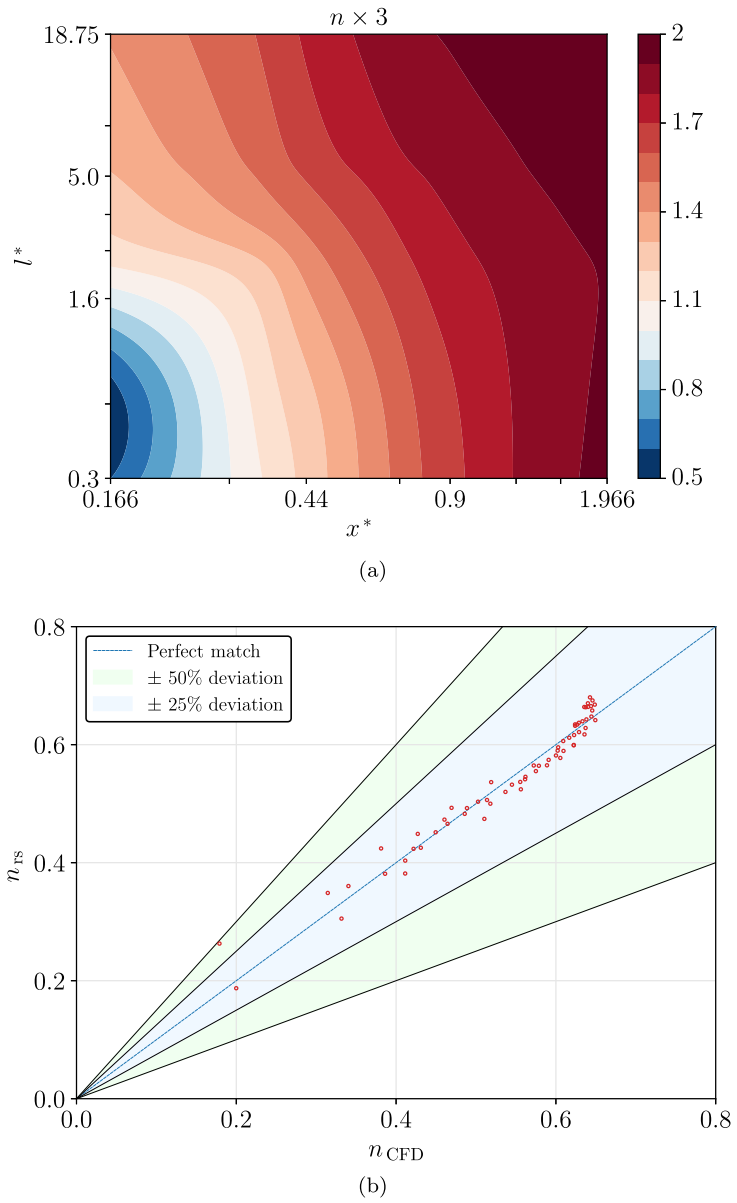

Fig. 13. Contour plot of the Prandtl scaling exponent obtained by CFD normalised by its canonical value of 1/3 (a) and deviations associated with the developed correlation (b). The x^* and l^* in (a) are scaled logarithmically, but the labels report linearly scaled values for improved readability.

for $\beta_r < 20\%$

$$j = e^{1.96}\,\alpha^{-0.098}\,\delta^{0.235}\,\gamma^{-0.154}\,\mathrm{Re}_{D_h}^{0.0634\ln\mathrm{Re}_{D_h}-0.623}\,\mathrm{Pr}^{0.0348} \tag{44}$$

for $20\% \le \beta_r < 25$

$$j = 1.06\,\alpha^{-0.1}\,\delta^{0.131}\,\gamma^{-0.08}\,\mathrm{Re}_{D_h}^{0.0323\ln\mathrm{Re}_{D_h}-0.856}\,\mathrm{Pr}^{0.0532} \tag{45}$$

for $25\% \le \beta_r < 30\%$

$$j = e^{1.3}\,\alpha^{0.004}\,\delta^{0.251}\,\gamma^{-0.031}\,\mathrm{Re}_{D_h}^{0.0507\ln\mathrm{Re}_{D_h}-1.07}\,\mathrm{Pr}^{0.051} \tag{46}$$

for $30\% \le \beta_r \le 35\%$

$$j = 0.2\,\alpha^{-0.125}\,\delta^{0.21}\,\gamma^{-0.069}\,\mathrm{Re}_{D_h}^{0.0005\ln\mathrm{Re}_{D_h}-0.338}\,\mathrm{Pr}^{0.0549} \tag{47}$$

Also in this case, when possible, the results coming from the correlations have been suitably scaled to adapt them to the reference quantities selected in this work. The explicit calculation of the Prandtl number exponent allows for a perfect alignment of the Colburn factors in turbulent regime, while considerable jumps occur near the laminar-turbulent transition. It is very interesting to note that with decreasing offset length and pitch, the discontinuity between laminar and turbulent results tends to be less pronounced until it almost disappears for the configuration with $x^* = 0.166$ and $l^* = 0.3$. Although the Prandtl number exponent was computed from results associated with Pr-values of 0.71 and 7, it represent an excellent approximation for scaling results referred to the much higher value of Prandtl number of 190, provided that they refer to a turbulent flow. This can be noted by examining the Colburn factor values obtained at Re = 500 and Pr = 190, which are perfectly aligned with water and air results. These results suggests that, in offset-strip fins, the Prandtl number exponent is most influenced by the flow regime and that this behaviour is very sensitive to the geometric configuration. On the other hand, if n is computed from reliable results, it can be considered valid over a large Prandtl number range, that effectively covers all the fluids of interest when dealing with compact heat exchangers.

In general, the correlations from the literature represent an acceptable approximation for the numerical results obtained in turbulent flow conditions and for small pitch and offset length values, while the deviations tend to increase with growing x^* and l^*. In laminar

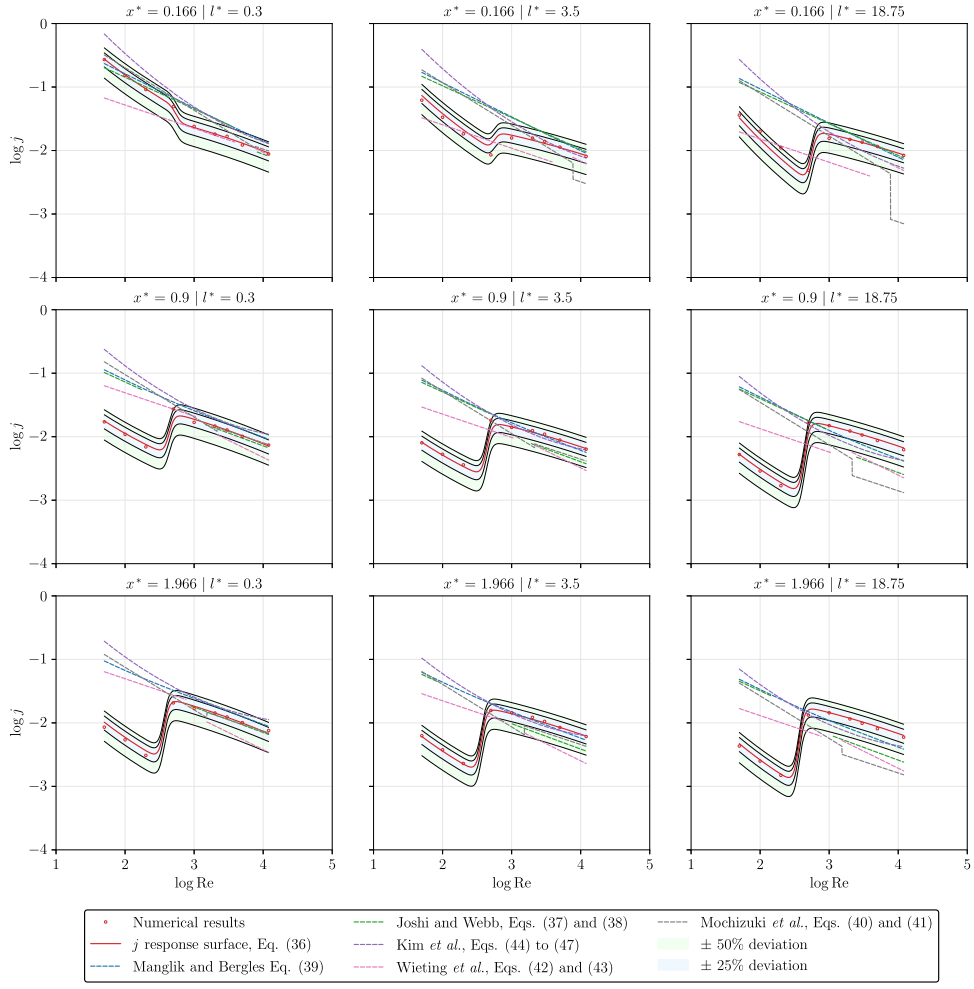

Fig. 14. Colburn factor: numerical results, developed response surface, and a comparison with the most relevant correlations from the literature for nine selected geometric configurations.

regime most of the correlations from the literature tend to greatly overestimate the Colburn factor for most of the geometric configurations. Nevertheless, it should be emphasised that most of these correlations were derived from experimental tests and CFD simulations related to air flows, and they were obtained by using the canonical value of 1/3 for the Prandtl scaling exponent, therefore large deviations should be expected [23,24].

The Colburn factor response surface developed in this work is in good agreement with the numerical results, as shown by the plot of Fig. 15(b). The mean deviation between the numerical results and the response surface is 8.3%.

6.3. Validation

The obtained response surfaces are validated by computing the internal head losses and overall heat transfer rates of three heat exchangers equipped with offset-strip fins, and comparing the results with the available experimental data. The examined units are oil coolers intended for lubricating or hydraulic oils, their external geometry is depicted in the drawing of Fig. 16(a), along with their most relevant dimensions: the height H, the main channel length L, the width of the two manifolds W, and the thickness S. The dimensional values of the coolers are reported in Table 7, along with an identification acronym for future reference. A picture depicting one of the actual heat exchangers is shown in Fig. 16. The internal channels of the three oil coolers feature the same exact offset-strip fin geometry, with a height of $y = 3$ mm, a pitch of $x = 1.5$ mm, an offset length of $l = 5$ mm, and a wall thickness of $t = 0.2$ mm. The front and top views of the internal fin are depicted in the drawing of Fig. 17(a), together with the previously listed dimensions. In the external channels of each cooler, wavy fins are employed to enhance heat transfer. They feature a triangular cross section and their geometry is shown in the drawing of Fig. 17(b), along with the main dimensions.

Table 7
External dimensions of the Geometrical parameters of the three examined oil coolers.

ID	S [mm]	H [mm]	W [mm]	L [mm]	N_{ch}
O80	80	304	60	500	20
O94	94	309	60	500	21
O113	113	305	60	500	20

The internal losses and overall heat transfer rates associated to the three oil coolers are evaluated by following the approach presented in [47], and by substituting the correlations for the offset-strip fin in Fig. 17(a) that were derived in [47] with the response surfaces developed in the present work. The internal losses are computed as the sum of the losses of the internal channels, which are modelled as a distributed loss via the Darcy-Weisbach formula, and the two concentrated losses modelling the effects of the inlet and outlet manifolds. The

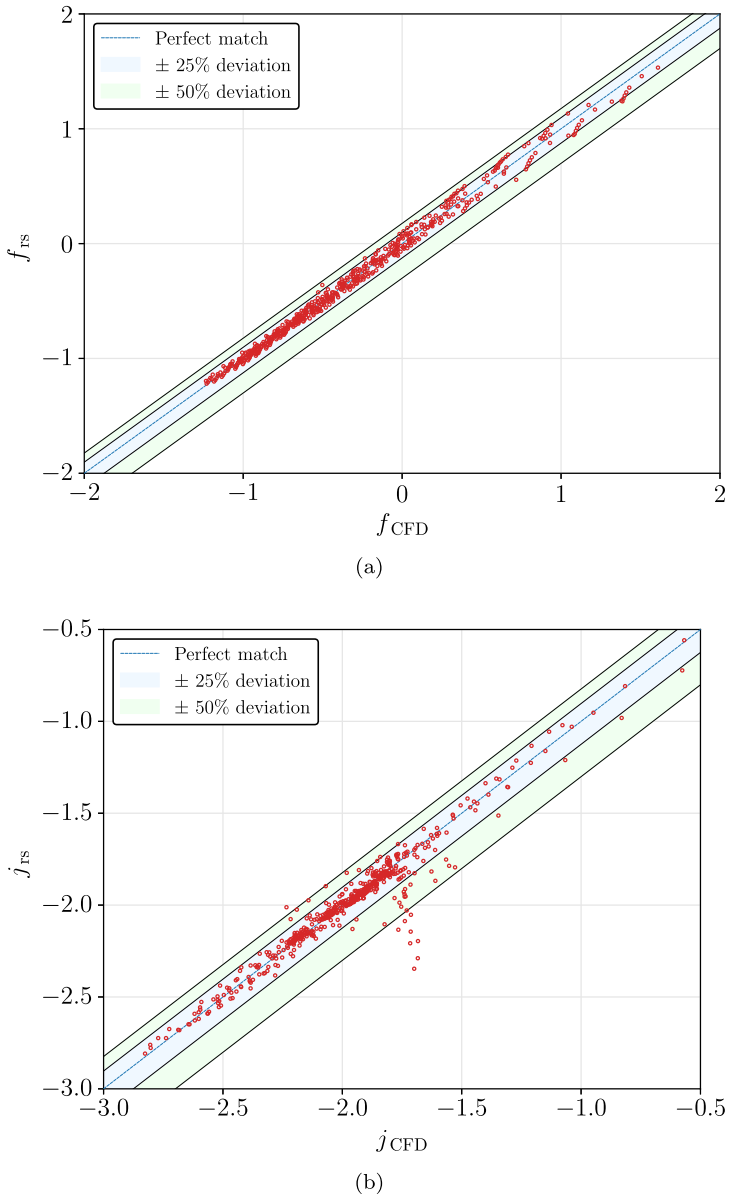

Fig. 15. Deviations between numerical results and estimations from the derived response surfaces for the equivalent Darcy friction factor (a) and Colburn factor (b).

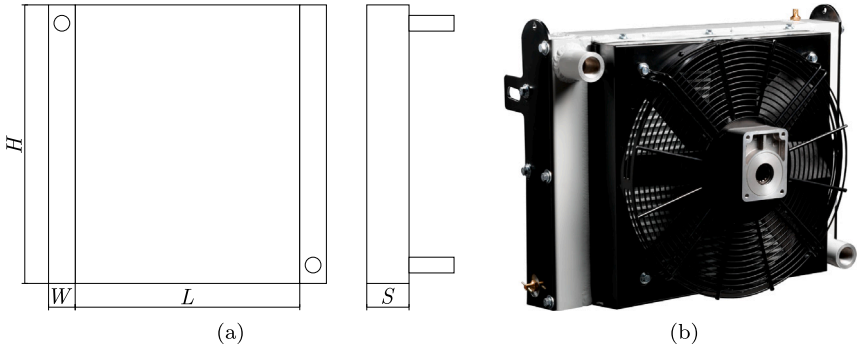

Fig. 16. Schematic of the external geometry and relevant dimensions of the three examined oil coolers (a) and an actual picture of one of the tested coolers (b).

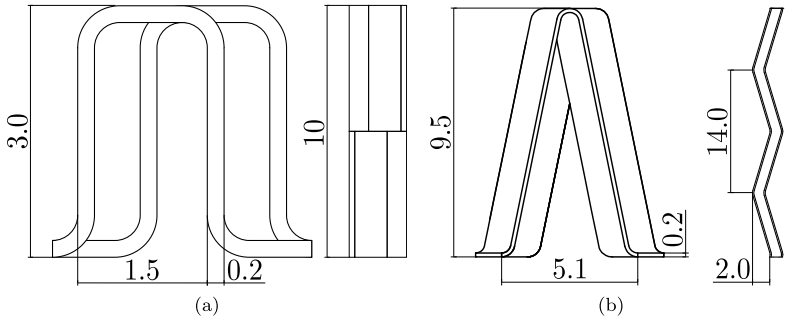

Fig. 17. Drawings depicting the front and top views of the offset-strip (a) and wavy (b) extended surfaces employed in the internal and external channels, respectively.

overall internal losses are given by:

$$\Delta p = \frac{1}{2}\rho\left(\beta_{\mathrm{i}}\, u^2_{\mathrm{i,he}} + f\,\frac{L}{y}\, u^2_{\mathrm{ch}} + \beta_{\mathrm{o}}\, u^2_{\mathrm{o,he}}\right) , \tag{48}$$

where β_{i} and β_{o} are the concentrated loss coefficients related to the inlet and outled manifolds, respectively. These are derived from the results of CFD analyses performed on these exact heat exchangers [47]. As previously mentioned, the friction factor in Eq. (48) is obtained from the response surface derived in Section 6.1, i.e. Eq. (13).

The heat transferred between the two fluids is assessed by the $\varepsilon-\mathrm{NTU}$ method assuming uniform heat transfer coefficients. The global heat transfer coefficient and surface area product is obtained from the series of the internal and external thermal resistances:

$$UA = \frac{1}{R_{\mathrm{int}} + R_{\mathrm{ext}}} = \frac{1}{\dfrac{1}{U_{\mathrm{int}}\, A_{\mathrm{int}}} + \dfrac{1}{U_{\mathrm{ext}}\, A_{\mathrm{ext}}}} . \tag{49}$$

The internal heat transfer coefficient U_{int} is computed by means of the Colburn factor response surface derived in this work (Eq. (36)). On the other hand, the external one is computed from the CFD derived correlations proposed in [47]. Finally, the effectiveness of the three oil coolers is computed under the hypothesis of unmixed fluids in a cross flow arrangement:

$$\varepsilon = 1 - \exp\left[\frac{C_{\max}}{C_{\min}}\mathrm{NTU}^{0.22}\left\{\exp\left[-\frac{C_{\min}}{C_{\max}}\mathrm{NTU}^{0.78}\right] - 1\right\}\right] . \tag{50}$$

The three oil coolers were also the subject of experimental tests that were carried out at the wind tunnel of Virtual Vehicle Research GmbH, during which the values of the internal head losses and the overall heat transfer rates were measured for several values of the internal and external flow rates. Please refer to [47] for further details.

Fig. 18 shows the comparison between the numerical results obtained in the present work, the corresponding results from [47] and the experimental data, regarding internal head losses and heat transfer rates. In these plots the values of pressure drop and heat transfer rate are scaled by their respective maximum experimental value. Numerical and experimental results are in very good agreement, as in both plots almost all the tested points feature deviations lower than 20%. On average, the deviation between the numerical and experimental values of the heat transfer rate is 8.8%, which is a slight improvement over the numerical results from [47], that feature a mean deviation of 9.9% with respect to the experimental data. The mean deviation between the numerical and experimental results on internal head losses is of 6.8%. These results are particularly noteworthy, since the response surfaces developed in this work were obtained considering only nominal geometric data and close to ideal fin geometries. On the other hand, finned surfaces in actual heat exchangers may feature severe shape deformations and residual metal scraps resulting from the manufacturing process, which, aside from experimental uncertainties, may be the major cause of deviations between numerical and experimental results. The response surfaces developed in this work allow for obtaining numerical results that, on average, are as accurate as the ones obtained from dedicated CFD analyses, thus corroborating the validity of the analysis presented in this work.

7. Concluding remarks

In this work, a comprehensive study on the heat transfer and friction properties of offset-strip fins with vertical walls, radiused corners, and centred offset was presented. The dependence of the equivalent Darcy friction factor f and Colburn factor j on geometric and flow parameters was evaluated through a DOE procedure, where each configuration was studied by CFD analysis of a periodic fin module. Numerical results were used to derive response surfaces for f and j with well defined applicability ranges, improving on the correlations available in the literature, which are developed on configuration sets that are highly unevenly distributed over the design space. The derived response surfaces showed mean accuracy values of ±8.4% with respect to the CFD results, and mean and maximum deviations of ±7.8% and ±20%, when validated against experimental data on complete heat exchangers. Novel results on the effect of the Prandtl number on heat transfer performance were also provided through the direct calculation of the Pr scaling exponent, n, from numerical results. These results showed that, at least in the case of offset-strip fins, the common assumption of $n = 1/3$, typical of the Chilton-Colburn analogy and used in the vast majority of studies, can be regarded as valid and accurate only for a small subset of geometric configurations, and that n varies significantly as a function of the geometric parameters. Hence, for this specific case, an original correlation for the Prandtl scaling exponent was proposed here. In conclusion, the novel data and correlations proposed in the present work are expected to have a positive impact on the design and performance assessment of heat exchangers with offset-strip fins. Furthermore, the predictive model proposed for the Prandtl scaling exponent represents a promising approach to accurately and systematically model Prandtl number effects on heat transfer effectiveness.

Declaration of competing interest

The authors declare the following financial interests/personal relationships which may be considered as potential competing interests: Diego Angeli reports a relationship with VEMA Industries S.p.A that includes: funding grants. Luigi Calò reports a relationship with VEMA Industries S.p.A that includes: employment. If there are other authors, they declare that they have no known competing financial interests or personal relationships that could have appeared to influence the work reported in this paper.

Data availability

The data that has been used is confidential.

Appendix A

The flow cross-sectional area of the considered OSF geometry equates to:

$$A_f = 2\,x\,y - A_w\,, \tag{A.1}$$

where A_w stands for the portion of frontal area occupied by the fin walls:

$$\begin{aligned} A_w = {} & 2r^2\left[\arcsin\left(\frac{c}{r}\right) - \frac{\pi}{2} - \arcsin\left(\frac{c-r}{r}\right)\right] \\ & + 2c\left[\sqrt{r^2-c^2} - (c-r)\sqrt{\frac{2r}{c}-1}\right] \\ & + 2t\left(y - \frac{\pi+2}{2}t + \pi r\right). \end{aligned} \tag{A.2}$$

The wetted perimeter is given by:

$$\begin{aligned} P = {} & 4\left\{x + y + r\left[\pi - 2 - \arcsin\left(\frac{\sqrt{2rc-c^2}}{r}\right)\right]\right\} \\ & - 2\pi t - 4\sqrt{2rc-c^2}\,. \end{aligned} \tag{A.3}$$

The heat transfer area A_{ref} consists of the whole fluid-solid interface of the fins, including leading and trailing edges, along with the area wetted by the fluid on the upper and lower horizontal surfaces:

$$A_{ref} = 2\,l\,P + 4\,(A_w - 2\,A_{ov})\,, \tag{A.4}$$

where A_{ov} is the portion of fin walls frontal area given by the overlap of two successive single fins.

$$\begin{aligned} A_{ov} = {} & r^2\left[\arcsin\left(\frac{c+t-r}{r}\right) - \arcsin\left(\frac{c-r}{r}\right)\right] \\ & + (c+t-r)\sqrt{(t+c)(2r-c-t)} \\ & + (r-c)\sqrt{2rc-c^2} \end{aligned} \tag{A.5}$$

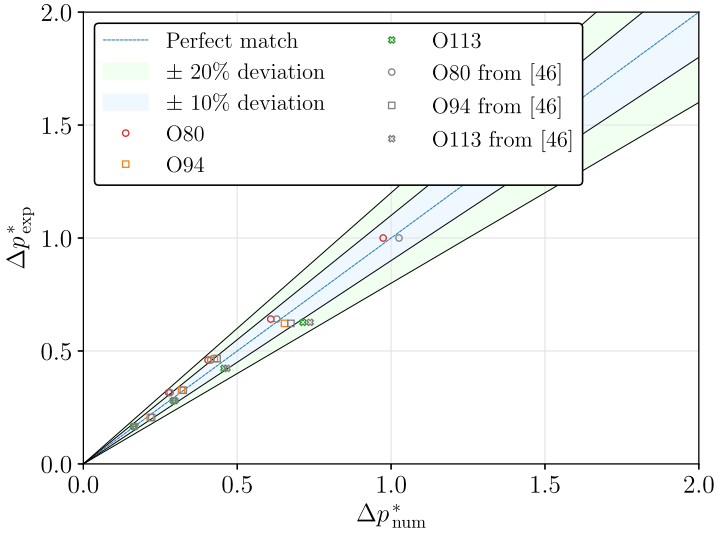

(a)

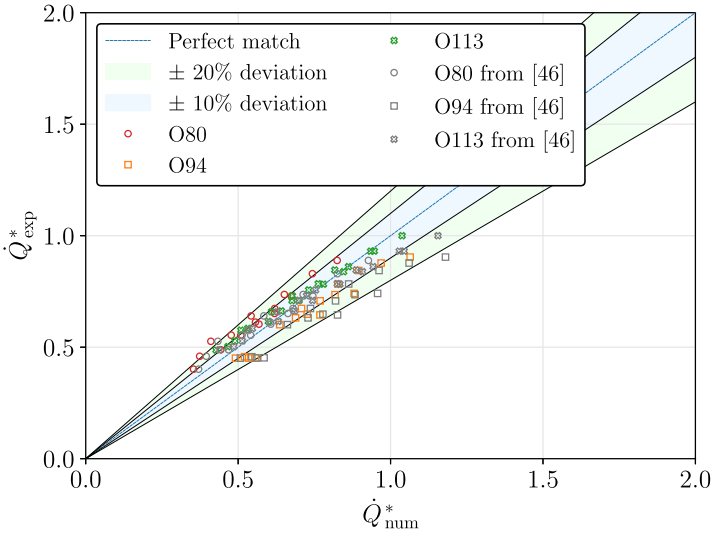

(b)

Fig. 18. Comparison between the numerically obtained values of internal head losses (a) and heat transfer rates (b) with the numerical results from [47] and the available experimental data.

Appendix B

```
/*--------------------------------*- C++ -*----------------------------------*\
| =========                 |                                                 |
| \\      /  F ield         | OpenFOAM: The Open Source CFD Toolbox           |
|  \\    /   O peration     | Version:  7.0                                   |
|   \\  /    A nd           | Web:      www.OpenFOAM.org                      |
|    \\/     M anipulation  |                                                 |
\*---------------------------------------------------------------------------*/
FoamFile
{
    version     2.0;
    format      ascii;
    class       dictionary;
    location    "constant/fluid-cells";
    object      thermophysicalProperties;
}
// * * * * * * * * * * * * * * * * * * * * * * * * * * * * * * * * * * * * * //

#include "../../initialConditions"

thermoType
{
    type                heRhoThermo;
    mixture             pureMixture;
    transport           const;
    thermo              hConst;
    equationOfState     rhoConst;
    specie              specie;
    energy              sensibleEnthalpy;
}

mixture
{
    specie
    {
        nMoles          1;   // placeholder
        molWeight       1;   // placeholder
    }
    thermodynamics
    {
        Cp              #calc "$Re*$Pr";
        Hf              0;
    }
    transport
    {
        mu              #calc "1.0/$Re";
        Pr              $Pr;
    }
    equationOfState
    {
        rho             1;
    }
}

// ************************************************************************* //
```

References

[1] O.O. Fadodun, O.G. Fadodun, A. Kaood, Hydrothermal performance and entropy production rate of rgo-co3o4/h2o hybrid nanofluid in corrugated-converging pipes, Int. J. Therm. Sci. 199 (2024) 108911.

[2] M.A. Hassan, A. Kaood, Multi-criteria assessment of enhanced radiant ceiling panels using internal longitudinal fins, Build. Environ. 224 (2022) 109554.

[3] W.M. Kays, A.L. London, Compact Heat Exchangers, third ed., McGraw-Hill, 1984.

[4] A.L. London, R.K. Shah, Offset rectangular plate-fin surfaces—Heat transfer and flow friction characteristics, J. Eng. Power 90 (3) (1968) 218–228.

[5] S.V. Manson, Correlations of Heat-Transfer Data and of Friction Data for Interrupted Plane Fins Staggered in Successive Rows, Technical Report, NASA, 1950.

[6] A.R. Wieting, Empirical correlations for heat transfer and flow friction characteristics of rectangular offset-fin plate-fin heat exchangers, ASME J. Heat Mass Transf. 97 (3) (1975) 488–490.

[7] H.M. Joshi, R.L. Webb, Heat transfer and friction in the offset stripfin heat exchanger, Int. J. Heat Mass Transfer 30 (1) (1987) 69–84.

[8] W.J. Yang S. Mochizuki, Y. Yagi, Transport phenomena in stacks of interrupted parallel-plate surfaces, Exp. Heat Transfer 1 (2) (1987) 127–140.

[9] E.V. Dubrovsky, V.Y. Vasiliev, Enhancement of convective heat transfer in rectangular ducts of interrupted surfaces, Int. J. Heat Mass Transfer 31 (4) (1988) 807–818.

[10] R.M. Manglik, A.E. Bergles, Heat transfer and pressure drop correlations for the rectangular offset strip fin compact heat exchanger, Exp. Therm Fluid Sci. 10 (2) (1995) 171–180, Aerospace Heat Exchanger Technology.

[11] S. Roesler, B. Kerler, J. Kuehndel, S. Forker, Experimental and numerical investigation of flow instabilities in offset strip fin heat exchanger geometries, in: International Heat Transfer Conference Digital Library, Begel House Inc., 2023.

[12] J. Dong, J. Chen, Z. Chen, Y. Zhou, Air-side thermal hydraulic performance of offset strip fin aluminum heat exchangers, Appl. Therm. Eng. 27 (2007) 306–313.

[13] M.S. Kim, J. Lee, S.J. Yook, K.S. Lee, Correlations and optimization of a heat exchanger with offset-strip fins, Int. J. Heat Mass Transfer 54 (9) (2011) 2073–2079.

[14] M.S. Kim, K.S. Lee, The thermoflow characteristics of an oscillatory flow in offset-strip fins, Numer. Heat Transfer A 58 (11) (2010) 835–851.

[15] Y. Yang, Y. Li, General prediction of the thermal hydraulic performance for plate-fin heat exchanger with offset strip fins, Int. J. Heat Mass Transfer 78 (2014) 860–870.

[16] Y. Yang, Y. Li, B. Si, J. Zheng, Performance evaluation of heat transfer enhancement in plate-fin heat exchangers with offset strip fins, Physics Procedia 67 (2015) 543–550, Proceedings of the 25th International Cryogenic Engineering Conference and International Cryogenic Materials Conference 2014.

[17] Y. Yang, Y. Li, B. Si, J. Zheng, R. Kang, Analysis of the fin performance of offset strip fins used in plate-fin heat exchangers, J. Heat Transfer 138 (10) (2016) 101801.

[18] F.P. Incropera, D.P. DeWitt, T.L. Bergman, A.S. Lavine, et al., Fundamentals of Heat and Mass Transfer, Vol. 6, Wiley, New York, 1996.

[19] H. Peng, X. Ling, J. Li, Performance investigation of an innovative offset strip fin arrays in compact heat exchangers, Energy Convers. Manage. 80 (2014) 287–297.

[20] G.J. Michna, A.M. Jacobi, R.L. Burton, An experimental study of the friction factor and mass transfer performance of an offset-strip fin array at very high reynolds numbers, J. Heat Transfer (2007).

[21] Y.S. Muzychka, M.M. Yovanovich, Modeling the f and j characteristics for transverse flow through an offset strip fin at low reynolds number, J. Enhanc. Heat Transfer 8 (4) (2001) 243–259.

[22] F.V. Tinaut, A. Melgar, A.A.R. Ali, Correlations for heat transfer and flow friction characteristics of compact plate-type heat exchangers, Int. J. Heat Mass Transfer 35 (7) (1992) 1659–1665.

[23] K.E. Herold, S. Hu, Prandtl number effect on offset fin heat exchanger performance: predictive model for heat transfer and pressure drop, Int. J. Heat Mass Transfer 38 (1995) 1043–1051.

[24] S. Hu, K.E. Herold, Prandtl number effect on offset fin heat exchanger performance: experimental results, Int. J. Heat Mass Transfer 38 (6) (1995) 1053–1061.

[25] L. Guo, J. Chen, F. Qin, Z. Chen, W. Zhang, Empirical correlations for lubricant side heat transfer and friction characteristics of the hpd type steel offset strip fins, Int. Commun. Heat Mass Transfer 35 (2008) 251–262.

[26] L. Guo, F. Qin, J. Chen, Z. Chen, Y. Zhou, Influence of geometrical factors and pressing mould wear on thermal-hydraulic characteristics for steel offset strip fins at low reynolds number, Int. J. Therm. Sci. 46 (12) (2007) 1285–1296.

[27] L. Guo, F. Qin, J. Chen, Z. Chen, Lubricant side thermal–hydraulic characteristics of steel offset strip fins with different flow angles, Appl. Therm. Eng. 28 (2008) 907–914.

[28] H. Xiang, W. Du, J. Zhao, Numerical investigation on the thermal-hydraulic performance of high prandtl number fluid in offset strip fin with different offset, Int. J. Heat Mass Transfer 220 (2024) 124915.

[29] J. Du, M.N. Yang, S.F. Yang, Correlations and optimization of a heat exchanger with offset fins by genetic algorithm combining orthogonal design, Appl. Therm. Eng. 107 (2016) 1091–1103.

[30] N. Kedam, D.A. Uglanov, E.V. Blagin, A.A. Gorshkalev, R.A. Panshin, J. Liu, Unified ann model for heat transfer factor (j) and friction factor (f) prediction in offset strip and wavy fin pfhes, Case Stud. Therm. Eng. 53 (2024) 103845.

[31] K. Chandan, K.V. Nagaraja, F. Gamaoun, T.V. Smitha, N. Neelima, Umair Khan, A.M. Hassan, Improving flow efficiency in micro and mini-channels with offset strip fins: A stacking ensemble technique for accurate friction factor prediction in steady periodically developed flow, Case Stud. Therm. Eng. 56 (2024) 104232.

[32] M. Salman, P. Dhamodharan, R. Prabakaran, S.C. Kim, Condensation heat transfer performance of r290 in a plate heat exchanger for electric vehicle heat pumps, Int. J. Therm. Sci. 203 (2024) 109103.

[33] J. Kim, Y. Park, H. Choi, J. Oh, H. Lee, Analyses of the thermal and hydraulic characteristics of a perpendicular-flow offset-strip-fin heat exchanger for electric vehicles, Int. J. Heat Mass Transfer 226 (2024) 125520.

[34] B. Kim, B. Sohn, An experimental study of flow boiling in a rectangular channel with offset strip fins, Int. J. Heat Fluid Flow 27 (3) (2006) 514–521.

[35] B. Pulvirenti, A. Matalone, U. Barucca, Boiling heat transfer in narrow channels with offset strip fins: Application to electronic chipsets cooling, Appl. Therm. Eng. 30 (14) (2010) 2138–2145.

[36] C. Ranganayakulu, S. Kabelac, Boiling of r134a in a plate-fin heat exchanger having offset fins, J. Heat Transfer 137 (12) (2015) 121002.

[37] R. Prabakaran, M. Salman, P.G. Kumar, D. Lee, S.C. Kim, Heat transfer and pressure drop characteristics of r1234yf during evaporation in a plate heat exchanger with offset strip fins: An experimental study, Int. J. Heat Mass Transfer 194 (2022) 123091.

[38] R. Prabakaran, M. Salman, D. Lee, S.C. Kim, Condensation of r1234yf in a plate heat exchanger with an offset strip fin flow structure for electric vehicle heat pumps, Int. Commun. Heat Mass Transfer 143 (2023) 106699.

[39] M. Salman, P. Dhamodharan, R. Prabakaran, S.C. Kim, Condensation heat transfer characteristics of low gwp r290/r1270 blend in a plate heat exchanger for ev heat pumps, in: Korean Society of Automotive Engineers Fall Conference and Exhibition, 2023, p. 1818.

[40] P. Dhamodharan, M. Salman, R. Prabakaran, S.C. Kim, Comparative analysis of r290 and r1234yf cooling performance in offset strip-fin plate heat exchanger for electric-vehicle battery thermal management, Int. Commun. Heat Mass Transfer 157 (2024) 107708.

[41] X. Zheng, Z. Qi, A comprehensive review of offset strip fin and its applications, Appl. Therm. Eng. 139 (2018) 61–75.

[42] F.R. Menter, Two-equation eddy-viscosity turbulence models for engineering applications, AIAA J. 32 (8) (1994) 1598–1605, Cited by: 13968; All Open Access, Green Open Access.

[43] M.R. Pendar, J.C. Páscoa, R. Lima, Numerical investigation of automotive paint oven for improving the thermal efficiency, in: Fluids Engineering Division Summer Meeting, Vol. 85840, American Society of Mechanical Engineers, 2022, V002T05A032.

[44] H.G. Weller, G. Tabor, H. Jasak, C. Fureby, A tensorial approach to computational continuum mechanics using object-oriented techniques, Comput. Phys. 12 (6) (1998) 620–631.

[45] S.V. Patankar, D.B. Spalding, Paper 5 - a calculation procedure for heat, mass and momentum transfer in three-dimensional parabolic flows, in: S.V. Patankar, A. Pollard, A.K. Singhal, S.P. Vanka (Eds.), Numerical Prediction of Flow, Heat Transfer, Turbulence and Combustion, Pergamon, 1983, pp. 54–73.

[46] F. Crameri, Scientific colour maps, 2023.

[47] M. Grespan, A. Leonforte, M. Cavazzuti, L. Calò, D. Angeli, Accurate reduced-order modelling of plate-fin heat exchangers, in: International Heat Transfer Conference Digital Library, Begel House Inc., 2023.

[48] D.W. Marquardt, An algorithm for least-squares estimation of nonlinear parameters, J. Soc. Ind. Appl. Math. 11 (2) (1963) 431–441.

[49] P. Virtanen, et al., SciPy 1.0: Fundamental algorithms for scientific computing in python, Nat. Methods 17 (2020) 261–272.